A new strategy for the estimation of plume height from clast dispersal in various atmospheric and eruptive conditions

Eduardo Rossi[1], Costanza Bonadonna[1], Wim Degruyter[2]

[1] Department of Earth Sciences, University of Geneva, 13, Rue des Maraichers, CH-1205 Geneva, Switzerland.
[2] School of Earth and Ocean Sciences, Cardiff University, Park Place, Cardiff, CF10 3AT, UK

Abstract

Plume height is an important parameter routinely used to characterize and classify explosive eruptions. Though the strategies to estimate key eruption source parameters such as erupted volume and mass flow rate have evolved over the past few decades, the determination of plume height of past eruptions is still mostly based on empirical approaches that do not account for the new developments in plume modelling based on the interaction of plume and wind. Here we present a revised strategy for the retrieval of plume height from field data that accounts for key aspects of plume dynamics and particle sedimentation, which are: i) the effect of wind advection on the buoyant plume, ii) a new parameterization of the gravitational spreading of the umbrella cloud for distances smaller than the radius of the plume, iii) the effect of particle shape on particle sedimentation, iv) the effect of different atmospheric profiles in different climate zones, v) three-dimensional wind, temperature and pressure data, and vi) topography. In particular, as wind can alter the direction and rise height of the plume, new computed sedimentation patterns are more complex and result in non-linear and non-intuitive relationships between downwind and crosswind deposition. Our method is tested against observations of the 2011 eruption of Shinmoedake (Japan), the 1980 eruption of Mount St Helens (USA), and the 1991 eruption of Pinatubo (Philippines). These are well-constrained examples of small, intermediate, and high intensity eruptions, respectively. Intensity scenarios are introduced to account for the non-unique relation between plume height and particle sedimentation resulting from wind advection of volcanic plumes. We further demonstrate that needle-like and disk-like particle shapes can have downwind distances 36 to 70% larger than the equivalent spheres. In addition, we find that the effect of latitude on the determination of

[1] Email address: Eduardo.Rossi@unige.ch

plume height is more significant for low and intermediate intensity scenarios with a discrepancy between 7 and 20%.

Keywords (max 6): plume height, plume dynamics, gravitational spreading, isopleth maps, nomograms

1. Introduction

Determining eruptive source parameters (e.g. erupted volume, plume height, mass eruption rate) and evaluating the associated uncertainties is crucial to the characterization of eruption dynamics and the assessment of associated hazards (e.g. Bonadonna et al. 2015 and references therein). The increasing availability of plume and dispersal models and real-time measurements have resulted in a better description of volcanic phenomena and their impact; nevertheless, in many circumstances (e.g. past eruptions with no direct observations), field data represent the only means to reconstruct the eruptive source parameters. Unlike the determination of erupted volume, which has been addressed by several authors (e.g. Bonadonna and Costa, 2012; Bonadonna and Houghton, 2005; Burden et al., 2013; Fierstein and Nathenson, 1992; Nathenson, 2017; Pyle, 1989; Sulpizio, 2005), the determination of plume height from field data is still mostly based on the methodology introduced by Carey and Sparks (1986), hereafter *CS86,* and revised by Burden et al. (2011), hereafter *BPH11*.

CS86 provide a set of plots, referred to as nomograms, that allows plume height and wind speed to be derived from the downwind and crosswind ranges of isopleth contours associated with clast sizes between 8 and 64 mm and clast densities between 250 and 2500 $\frac{kg}{m^3}$. The method of CS86 is based on the definition of the clast support envelope, a region of the plume, outside of which, particles of a specific size may no longer be suspended within the plume and thus settle out. The simple application has made CS86 the most widely used method for the calculation of plume height within the community (e.g. BPH11 and references therein). BPH11 have already addressed a few important issue of the methodology introduced by CS86 by: i) using a plume model to avoid empirical relations for volume and temperature changes of the gas mixture along the column; ii) quantifying the associated uncertainties; iii) describing the radial velocities above the Neutral Buoyancy Level (NBL) based on a gravity current model, and iv) using more realistic wind profiles for the sedimentation of volcanic clasts in the atmosphere. Despite these important implementations, additional fundamental processes still need to be addressed.

The main goal of this work is to better characterise the key role of wind in defining clast support envelopes along the downwind direction. This results in a methodology for the determination of plume height from clast dispersal applicable under a large range of eruptive and atmospheric conditions. Moreover, we have implemented a new parameterization of the gravity current for distances smaller than the radius of the plume and characterized the influence of both particle shape and tropopause height on the final isopleth contours. Finally, we provide a new set of

nomograms that can be applied to a wide range of eruptive conditions and a Matlab script to facilitate their application (downloadable from the journal website). The complete Matlab package for detailed analyses of single eruptions and the computation of theoretical isopleth contours in case of eruptions with known wind field and topography is available on request.

2. New modelling strategy

Following CS86, our model requires two fundamental steps: first, the definition of a clast support envelope within the volcanic plume; second, the determination of the trajectories of falling particles released from the envelope margins. CS86 assume empirical approximations of volume and temperature changes in the gas mixture within the column that introduce a significant approximation. The revised methodology proposed by BPH11 improves this aspect, using a more sophisticated plume description based on the model of Woods (1988). However, in both these models, the effect of the horizontal momentum of the wind on the rising column is poorly constrained. According to Degruyter and Bonadonna (2012), the influence of atmospheric wind with a height-averaged velocity $\bar{V}_{wind}$ can be quantified with the parameter $\Pi \propto k \frac{\bar{N} H}{\bar{V}_{wind}} \left(\frac{\alpha_e}{\beta_e}\right)^2$, in which α_e and β_e are the radial and wind entrainment coefficients, $\bar{N}$ the height-averaged buoyancy frequency, H the maximum height of the plume centreline, and k a constant. Values of $\Pi \gg 1$ characterize *strong plumes*, i.e. eruptions dominated by the vertical plume rise, while values of $\Pi \ll 1$ imply a dominant influence of wind on plume rise (i.e. weak plumes), with a consequent effect on the shape of the clast support envelopes and, therefore, on the particle sedimentation distance (Fig. 1).

Once clasts are released from the envelope region, their deposition strongly depends on the wind velocity fields. Simplified sedimentation models are both present in CS86 and in BPH11. However, a more realistic trajectory for centimetric particles, i.e. characterized by Stokes number $St > 1$, is obtained solving the equation of motion for each particle (section 2.3), without assuming that the horizontal velocities of the clasts are equal to the external velocity fields. The Stokes number $St = \frac{\tau_p}{\tau_f}$ relates the response time of a particle, τ_p, with the characteristic timescale of the fluid τ_f (Jessop and Jellinek, 2014). As indicated in Fig. 2, we provide two strategies to determine plume height: i) from a compilation of nomograms in various eruptive and atmospheric conditions (a Matlab script is available on the journal website for a more accurate use of the plots) (inversion mode) or ii) from the direct application of a

dedicated Matlab package (available on request) accounting for better constrained eruptive information, atmospheric conditions and topographic data (forward mode).

2.1. Plume velocity field

To define a clast support envelope within a volcanic plume as prescribed in CS86, we first require the knowledge of the plume centreline velocity and the Gaussian cross-plume velocity profile. We first calculate the plume centreline velocity using the integral plume model of Degruyter and Bonadonna (2012, 2013), which assumes a top-hat profile. We then convert the cross-plume velocity to an equivalent Gaussian profile using the considerations of Davidson (1986). The governing equations of the integral model consider the balance of mass, momentum, and heat flow rates within a control volume. The model accounts for the effect of wind, which we expand to include variations in wind direction in the azimuthal plane following Folch et al. (2016). We summarize the model details in Supplementary Material S2. The complete list of mathematical symbols is instead available in Supplementary Material S5.

Gaussian and top-hat velocities, denoted by U_g and U_{th}, respectively, are related through averaging over the plume circular cross-sectional area:

$$U_{th} = \frac{1}{\pi R^2} \int_0^R U_g \, 2\pi r \, dr \tag{1}$$

with r the cross-plume radial distance from the plume centreline and R the top-hat radius. Following Davidson (1986), for a plume in an external constant wind field of value V_{wind} it holds that:

$$U_g(s,r) = V_{wind}(s,r)\cos\big(\theta(s)\big) + U_g^*(s)\, e^{-\frac{r^2}{b(s)^2}} \tag{2}$$

where s is the curvilinear coordinate along the trajectory, θ is the bending angle with respect to the horizontal axis, U_g^* is the velocity at the centre of the plume and b is the cross-plume radial distance at which the Gaussian velocity profile decays to $1/e$ of the centreline value. This expression defines the velocity difference between plume and wind along the central axis as a Gaussian function. In a real environment, the wind varies along r. We assume that V_{wind} is locally constant along the radial coordinate and equal to the value at the centre of the plume, i.e. $V_{wind}(s,r) = V_{wind}(s,0)$. The wind velocities at a given height z are interpolated from the closest points available in the atmospheric profile.

The characteristic width of the Gaussian velocity profile, b, can be expressed in relation to the top-hat radius R according to the following assumption (Davidson, 1986):

$$\frac{R^2}{b^2} = 2 \tag{3}$$

Therefore, using Eq. (2) and Eq. (3) inside equation Eq. (1), Gaussian velocities can be expressed in terms of their relative top-hat values:

$$U_g^*(s) = \frac{2\,(U_{th}(s) - V_{wind}(s)\cos\theta(s)\,)}{1 - e^{-\frac{R^2}{b^2}}} \approx 2\,(U_{th}(s) - V_{wind}(s)\cos\theta(s)\,) \tag{4}$$

where the approximation is commonly used in the literature (Davidson, 1986; Sparks, 1986). However, it is worth mentioning that this expression is exact only for integration over an infinite radius. Integrating over the radius R results in a relative error for U_g^* of about 14% with respect to the full equation.

2.2. Clast support envelope

The criterion used to define the clast support envelopes is based on the vertical motion of the particles and mean (time-averaged) plume motion. A single clast falling at terminal velocity will experience no net force if the surrounding air has an upward flow of equal magnitude. This equilibrium suggests that an upward flux generating a velocity field greater than the clast terminal velocity will exert sufficient drag such that the clast will approximately follow the same trajectory as the plume. When the terminal velocity of the particle is greater than the plume velocity, clasts are no longer coupled with the gas mixture and they start to sediment. The expression for the terminal velocity U_{tv} is:

$$U_{tv} = \sqrt{\frac{4}{3}\frac{\rho_c d\, g}{\rho_f C_d}} \tag{5}$$

where g is the gravitational acceleration, d particle diameter, ρ_c clast density, C_d is the drag coefficient and ρ_f is the density of the plume mixture to be evaluated at each height. Given their dependence on C_d, terminal velocities are calculated iteratively equating the gravity force and the drag force (see Appendix A.1). The buoyant force is neglected due to the large difference in density between clasts and surrounding gas. Thus, the clast support envelope is

defined as the three-dimensional surface where the vertical component of the plume velocity field equals the terminal velocity U_t of the clast (Fig. 1). Solving the equation $U_t = U_g \cdot \sin(\theta)$ for the unknown radius of the envelope, R_{env}, at a given height *z*, we find:

$$R_{env} = b \cdot \sqrt{-\ln\left\{\frac{1}{U_g^*}\left[\frac{U_{tv}}{\sin(\theta)} - V_{wind} \cdot \cos(\theta)\right]\right\}} \quad (6)$$

Clast support envelope is calculated as a post-process operation once that plume velocities are determined, as in CS86. As shown in Fig. 1, atmospheric winds strongly affect the shape of the envelope.

2.3. Particle sedimentation

Depending on the use of the model, i.e. for nomogram compilation (inversion mode) or for running single eruption scenarios (forward mode) (see Fig. 2), particles are respectively released from selected points (the most downwind and crosswind locations on each envelope ring) or from random points uniformly distributed over the surface of the envelope. We determine the maximum deposition distance along the downwind and crosswind axes. Initial velocities are set equal to zero and each trajectory is described in a fixed frame of reference with the origin situated on a release point on the support envelope and the axes oriented as shown in Fig. 1.

Clast trajectories in the atmosphere are determined in a Lagrangian framework considering the effects of the drag force $\vec{F}_{drag}$ and gravity force $\vec{F}_g$:

$$m_c \frac{d\vec{U}_c^i}{dt} = \vec{F}_{drag} + \vec{F}_g \quad (7)$$

where $\vec{F}_{drag} = \frac{1}{2}\,\rho_f\,A\,\left|\vec{U}_c^i - \vec{U}_f\right|(\vec{U}_c^i - \vec{U}_f)\,C_d$, $\vec{F}_g = m_c\vec{g}$, A is the projected area of the clast with a diameter d_c ($A \approx \frac{\pi}{4}d_c^2$), $\vec{U}_c^i$ is the velocity of clast *i*, $\vec{U}_f$ is the velocity of the surroundings and m_c is the mass of the object. At each time step, the drag vector is evaluated and then decomposed along the Cartesian axes in order to solve the motion in three-dimensional space. A more detailed analysis of the global forces acting on a clast in the atmosphere can be found in de' Michieli Vitturi et al. (2010). We assume that the forces that depend on the density ratio between solid particles and air, which is small, i.e. buoyancy and virtual mass term, and on the history of the trajectory (*Basset force*) are negligible.

The solution of Eq. (7) requires an expression for the drag coefficient C_d and the surroundings $\vec{U}_f$ along the particle trajectory. The drag coefficient is specified from the parameterization proposed by Bagheri and Bonadonna (2016) for non-spherical particles, which ensures a reduced average error of about $\sim 10\%$ with respect to the observed data (see Appendix A.1). The velocity field outside the volcanic column and umbrella cloud is determined by the atmospheric wind. Within the umbrella cloud, there is the additional contribution of gravitational spreading. Following CS86 and BPH11, we constrain the umbrella cloud region between the NBL and the top of the plume. The alternative description of gravity current spreading around NBL, e.g. between a minimum and maximum height of $\approx 0.8\, H_{NBL}$ and $\approx 1.2\, H_{NBL}$ (Bonadonna and Phillips, 2003) was also tested with no significant difference in the resulting sedimentation distances.

For consistency with CS86, two distinct regions of sedimentation are defined: sedimentation above the NBL (where the radial velocity field of the gravity current dominates over wind advection; see section 2.4) and sedimentation below the NBL (where the atmospheric wind is the only component contributing to clast lateral transport; see section 2.5). The resulting set of ODEs is solved using the Matlab solver ode45, an explicit Runge-Kutta algorithm of 4th-5th order (Shampine and Reichelt, 1997).

2.4. Gravity current above the Neutral Buoyancy Level (NBL)

In the region around the NBL (i.e. the umbrella cloud) the density difference between the volcanic mixture and the atmosphere produces radial spreading as a gravity current (e.g. Johnson et al. (2015)). For large eruptions, there is a relevant contribution of the gravity current to the total spreading rate of the umbrella cloud especially for proximal distances (Costa et al., 2013). The parameterization of the velocity of the gravity current U_{gc} is commonly based on the mass conservation of the incoming mass per unit time from the volcanic column and the consequent spreading of the current (Sparks, 1986). In addition, a relationship between the thickness h_{gc} and velocity of the gravity current can be defined based on scaling arguments (Bonadonna and Phillips, 2003). In both cases, this is mathematically consistent for distances greater than the plume radius at the NBL. For smaller distances, this approach overestimates the gravity-current velocity, and diverges to infinity when the distance approaches zero (Fig. 3). This aspect has some impact on plume modelling that follows the approach of CS86, since clasts are often released from regions inside the plume and above the NBL.

We propose a solution that comes from balancing the actual Mass Flow Rate Q^{NBL} (MFR) entering a given section at the NBL. For an object located inside the plume radius, the radial velocity at a distance r is generated by the actual MFR entering in a cross section πr^2, which tends to zero for $r \to 0$. If we assume that the velocity of the front of the gravity current scales as a function of the atmospheric buoyancy frequency N and a correction factor $\lambda \approx 1$ ($U_{gc} = \lambda N h_{gc}$) (Bonadonna and Phillips, 2003), we obtain:

$$U_{gc} = \left(\frac{\lambda N V_{wind}}{2} \cos(\theta)\, r + \frac{U_g^* \lambda N R^2}{4} \frac{(1 - e^{-\frac{r^2}{b^2}})}{r} \right)^{\frac{1}{2}} \quad with \quad 0 \le r \le \infty \tag{8}$$

Eq. (8) represents a generalization of gravity currents for a Gaussian profile of the plume velocity and for any distance.

A comparison of equation Eq. (8) with those presented in Sparks (1986) and Bonadonna and Phillips (2003) is shown in Fig. 3. The unrealistic high velocities commonly present in the previous works for small distances are replaced with a curve that drops to zero corresponding to a null radius. For $r = R_{NBL}$ the velocity calculated with Bonadonna and Phillips (2003) differs by about 7% from equation Eq. (8). This discrepancy tends rapidly to zero for increasing distances (Fig. 3).

2.5. Meteorological data

We use a flexible structure for the description of atmospheric conditions that can easily be modified. In the standard mode of operation, the code reads an Era-Interim dataset provided by the European Centre for Medium-Range Weather Forecasts (ECMWF) (Dee et al., 2011). This dataset is downloaded using a modified version of the software *TephraProb* (Biass et al., 2016). This mode of operation is used for all situations where complete meteorological information is available, namely for all eruptions that occurred later than 1979 (see Biass et al., 2016 for a more detailed description on the application of ECMWF data to volcanic eruptions). The default wind profile provided by CS86 is also available for all other cases. This profile assumes zero velocity on the ground and a linear increase up to the tropopause height, where it has its maximum value V_{wind}^{max}. It decreases linearly down to 0.75 V_{wind}^{max} in the stratosphere at a height H_S (Fig. 4b). Standard values of V_{wind}^{max} are chosen following CS86. A default value of 20 km is attributed to H_S. However, a variation of H_S between 14 km and 20 km does not affect significantly the final nomograms (the change in downwind ranges is less than 1%).

3. Comparison with existing models and with field observations

3.1. Comparison with existing dispersal models

Our new model is compared against the results of BPH11 (cf. Fig. 2 of BPH11) (Fig. 4). The maximum plume centreline height is expressed as a function of the maximum downwind range for particles with a diameter of 0.8 cm, a density of $2500\ kg/m^3$, and no wind. The ranges of parameters investigated covers the same ranges as in BPH11 (cf. their Table 1). Four quantities are varied: initial radius, gas mass fraction, initial velocity and temperature. Particles are released from the entire column with no preferential release point on the envelope. Fig. 4 shows a general agreement between our model and previous works, with two main differences: slightly smaller downwind distances for plume heights less than $\approx 15\ km$ and a wider variability of the heights for a fixed downwind distance. In our model, this last aspect can be explained due to the complex combination of radial spreading above the NBL and the effect of the initial radius on the exit velocity of the column. As a result, an envelope wider in horizontal extension but smaller in height can produce the same downwind distance as a much higher, but narrower, plume. This variability can be strongly reduced if eruptive scenarios are identified, so that eruptions with very different initial radii are not clustered together (see section 3.2.2).

3.2. Comparison with field data

A Lagrangian model (such as that presented here) cannot be easily validated with the values of the largest clasts resulting from a non-standardized average of a different number of axis and of particles as those available in literature (Bonadonna et al. 2013). As a result, we have carried out a quantitative comparison with field data based on two alternative procedures. First, isopleth contours computed with our new model are compared with values of the largest clasts collected from selected tephra deposits. Second, observed plume heights for selected eruptions are compared with plume heights predicted by our new nomograms.

3.2.1. Comparison between computed isopleth contours and field observations

Three eruptions with different intensity have been selected: the eruption of Pinatubo 1991, Philippines (Rosi et al., 2001) that was characterized by both intermediate winds and strong plume ($\Pi \approx 0.5$); the 1980 eruption of Mount St Helens, USA (Carey et al., 1990) that was characterized by strong wind and a transitional plume ($\Pi \approx 0.3$); and the 2011 eruption of

Shinmoedake, Japan, that was characterized by a strong wind and a weak plume ($\Pi \approx 0.04$) (Maeno et al., 2014). In this section, computed isopleth contours are compared with ground locations of the observed largest clasts. For all the three cases, we used the ECMWF meteorological data (Dee et al., 2011) that were the closest in time to the recorded date of the eruption. Ideally, we would expect computed isopleth contours associated with a given size to be outside (i.e. to contain) all locations of the observed largest clasts of the same size or larger and the maximum downwind and crosswind distances to match with the theoretical ones. However, a probabilistic approach is necessary since the maximum travelled distance of a clast is very sensitive to fluctuations in the eruptive parameters that are poorly constrained. Initial conditions are randomly picked from a uniform distribution within a given range (see table S1 in *supplementary materials*) and the values of MFR are chosen to recreate the plume heights reported in the literature. This probabilistic approach allows confidence intervals to be defined in the explored parameter space. Two thresholds of 5% and 95% are identified to compare independent field data and computed isopleth contours.

3.2.1.1. Mount Pinatubo 1991, strong plume

The 1991 eruption of Mount Pinatubo is one of the largest eruptions that occurred in the 20th century. During the 15th-16th of June, the plume reached the height of about 39 km above sea level (a.s.l.) (Holasek et al., 1996). This climactic phase is an example of a strong plume since the wind did not significantly affect the rise of the volcanic column. The range of initial conditions and parameters used for this set of simulations are reported in Table S1. Three sizes of lithic clasts are considered: 0.8, 1.6 and 3.2 cm to compare with the published data based on the average of the maximum dimension of the five largest clasts (Rosi et al., 2001). Fig. 5 shows a good agreement between modelled isopleth contours and field data. In particular, particles of 0.8 cm and 1.6 cm are all contained within their own confidence interval, which suggests a correct estimation of the downwind and crosswind distances. Results for the 3.2 cm particles tend to overestimate the sedimentation distance with respect to observations. The discrepancy can be due to the fact that the height of the clast support envelope for 3.2 cm particles matches the height at which wind abruptly changes direction. In the probabilistic approach, the simulations with a clast support envelope above the height of shift in wind direction smooth this sharp threshold. As a result, the strong wind shear produces a mismatch between model and observations for this specific particle size.

3.2.1.2. Mount St Helens 1980, transitional plume

Four phases were identified for the 18 May 1980 eruption of Mount St Helens: B1 and B2 phases associated with Plinian fallout; B3 phase, characterized by a pyroclastic density current (PDC) and associated co-PDC plumes; and B4 phase, characterized by a Plinian column up to 19 km a.s.l. (Carey et al., 1990). The comparison of our model is done with the lithic clasts (1 cm in diameter) of the B2 phase as reported in Carey et al. (1990) (associated plume height of about 13-15 km above the vent.; Holasek and Self 1995). This value is used as a reference for the simulations, leading to a reasonable MFR between $0.7 - 3 \times 10^8 \frac{kg}{s}$ (Degruyter and Bonadonna, 2012; Pouget et al., 2013). Fig. 6 shows a good agreement between computed isopleth contours for 1 cm sizes and field data with all the particles smaller than 1 cm plotting outside the confidence region.

3.2.1.3. Shinmoedake 2011, weak plume

Three sub-Plinian eruptions occurred at Mount Shinmoedake at 2.30pm (LT) of the 26th January 2011, at 2am (LT) of the 27th January 2011 and at 3.40pm (LT) of the 27th January 2011 (Maeno et al., 2014). During each of the three eruptions, the volcanic column reached an observed height of about 7 km above the vent (Maeno et al., 2014). The wind blew strongly towards southeast with a maximum intensity of 70 m/s at the tropopause (Suzuki and Koyaguchi, 2013). A sequence of meteorological profiles has been used to cover the time span from the onset to the end of the eruptive period. The observed largest clasts were determined based on the average of the 3 dimensions of the five largest clasts in a depositional plane of 0.5 m^2 at each outcrop (Maeno et al., 2014). The rapid increase of the eastward component of wind with height, combined with a major role of the gravity current for larger eruptions, results in a complex shape of the isopleth lines. However, the computed contours are generally in good agreement with field observations (i.e. pumice clasts of 0.9 cm in diameter; Fig. 7)

3.2.2. Comparison with observed plume heights based on the new nomograms

Following CS86, the resulting 3D plot showing downwind range vs. crosswind range vs. plume height is summarized in a 2D plot, i.e. the nomogram, obtained interpolating and extrapolating the information at predefined heights starting from our set of simulations (see Table S2 for eruptive conditions). Meteorological parameters are also described as a function of tropopause height and a default wind profile is expressed as a function of the maximum velocity at the tropopause. Four values of the wind velocity at the tropopause (V_{wind}^{max}) have been investigated:

0, 10, 20 and 30 m/s. Four sizes are initially considered for particles with a density of 2500 $\frac{kg}{m^3}$: 0.8 cm, 1.6 cm, 3.2 cm and 6.4 cm (and aerodynamic equivalent for different particle densities). In total, we have computed 12 nomograms (see Supplementary Material for sizes of 0.8 cm and 6.4 cm). Particles are assumed to be spherical, i.e. with flatness and elongation equal to one. We also consider the standard atmospheric profile, i.e. with a tropopause height of 11 km, a surface temperature of 288 K and an average adiabatic lapse rate of the temperature in the troposphere of $-6.5\ K/km$ (Champion & Cantor, 1985). However, we consider the effects of particle shape and arctic and tropical atmospheric profiles on the final nomograms in Appendix A and Supplementary Material, respectively.

Three main eruptive scenarios are defined for the compilation of nomograms mostly based on MFR and initial plume radius: *low intensity*, with radii less or equal to 50 m; *intermediate intensity*, with radii comprised between 50 and 200 m; *high intensity*, with radii comprised between 200 and 500 m (see Table S2 in Supplementary Material for more details). The choice of these three scenarios is in line with the three case studies considered: the *low intensity scenario* can be applied to events with similar (or smaller) MFR to the 2011 eruption of Shinmoedake volcano, Japan; the *intermediate intensity scenario* can be applied to events similar to 1980 eruption of Mount St Helens, USA; the *high intensity scenario* can be applied to events similar or larger than the 1991 eruption of Mount Pinatubo, Philippines.

The identification of plume scenarios helps differentiate eruptions associated with similar downwind and crosswind ranges but different initial conditions (i.e. mostly plume radius and MFR). As a matter of fact, the final deposition distance is a complex function of the shape of the clast support envelope and the sedimentation trajectory above and below the NBL. Two eruptions with different MFR and vent radii can be characterized by different envelopes but not necessarily by different downwind and crosswind distances, if the effects of the gravity currents and the wind are considered. The use of three nomograms (associated with the three scenarios of initial eruptive conditions) for each particle size reduces considerably the uncertainties associated with the identification of plume height, if some constraints on the eruption are a priori known, such as expected intensity (small, intermediate or high) based on geometry and extension of isopleth and isopach maps.

Table1 shows how most plume heights predicted with the nomograms of CS86 are higher than those predicted with the nomograms of Figs 8 and 9. It is important to note that a correct comparison of results from both the nomograms of CS86 and those presented in this work is to be carried out with the height of plumes above sampling heights (i.e. column 3 in Table1) and

not relatively to the vent or sea level (as calculated heights are relative to the location where clasts have deposited). In general, heights predicted with the new nomograms show a good agreement with those observed above sampling area, with a maximum and average relative discrepancy of 25% and 7%, respectively (Table 1, column 4). In contrast, both the maximum and the average relative discrepancies resulting from the application of CS86 are higher (i.e. 31% and 15%, respectively). We should also consider that the absolute discrepancy in the determination of plume height is within 2 km using the nomograms of Figs 8 and 9 and within 7 km using the nomograms of CS86. Finally, complex wind profiles (such as that associated with the Shinmoedake eruption) cannot be easily captured by the standard nomograms presented in this work (Figs 8 and 9) and by those of CS86, in which case the use of the complete model is recommended.

For a fixed intensity scenario, nomograms are obtained averaging the outcomes of simulations with different initial plume radii, as in Table S2 (Supplementary Material). This process unavoidably produces a set of different plume heights for a given pair of downwind and crosswind ranges in the nomogram. We quantified this variability evaluating the average, the minimum and the maximum plume heights for several pairs of downwind and crosswind ranges. The difference of maximum and minimum heights has been normalized to the average. Finally, we took the median of all the relative differences as a good unbiased indicator of the variability in a nomogram. We found that low intensity scenarios have smaller values of variability ($\approx 6\%$) respect to intermediate ($\approx 17\%$) and large intensity ones ($\approx 25\%$).

A crucial aspect is that plume heights computed with the new nomograms are generally lower (between 5% and 23%) than those obtained with CS86 for the cases reported in Table 1. As expected, this is due to the contribution of the tilted envelope on the sedimentation distances. Tilted envelopes can produce significant sedimentation distances even for small plume heights. However, in CS86 remarkable values of downwind ranges are associated with remarkable plume heights. The contribution of the initial position along the downwind axis for clasts released from a tilted envelope is only approximatively taken into account, due to their simplified description of the interaction of wind and the volcanic plume.

For most eruptions the intermediate intensity scenario produces the best result. This is expected since this scenario spans a range of vent radii that is typical for most steady, explosive volcanic eruptions. The observed plume height for Mount Pinatubo ($z_{max} \approx 39\ km$ a.s.l.) is in between the predictions of the intermediate intensity ($z_{max} = 37\ km$ a.s.l.) and the high intensity ($z_{max} = 42\ km$ a.s.l.) scenarios. Consequently, we deduce that the high intensity scenario is representative of very large events (e.g. ultra-Plinian eruptions), even larger than the

1991 Pinatubo eruption. This consideration should facilitate the practical use of the nomograms of Figures 8 and 9.

4. Discussion

4.1. Advantages of the new model

The approach presented in this paper proposes a step forward in the methodologies of CS86 and BPH11. The first significant advantage is the use of tilted envelopes in presence of weak and transitional plumes (see Degruyter and Bonadonna (2012) and Bonadonna et al. (2015)). If we compare the nomograms calculated in this study with those of CS86, we notice that the straight lines representing plumes with a fixed height are now replaced by inclined curves that rise as the downwind range increases. Eruptions characterized by downwind range larger than a fixed crosswind range are generally attributed to lower heights with respect to CS86. However, weak and transitional plumes are characterized by a non-negligible bending of the column along the wind direction. Therefore, particles may be released from the plume at a significant distance from the vent. As a result, large downwind ranges could be erroneously attributed to significantly higher plumes if the effect of the wind on the column is not adequately taken into account.

Second, in the new model the full equation of motion is solved for each particle, i.e. sedimenting particles do not immediately move at their terminal velocity. In addition, for eruptions that occurred after 1979, the model can take advantage of three-dimensional meteorological profiles, time and space dependent. For historical eruptions, a standard wind profile is adapted to the entire grid following CS86. This implementation allows also for the description of dynamic wind profiles for long-lasting eruptions (e.g. 2011 Shinmoedake eruption; Fig. 7).

Third, even though the nomograms have been compiled for spherical particles, the present model can also account for the effect of particle shape on settling velocity. In particular, the description of the drag coefficient allows for the description of particle flatness and elongation as specified in Bagheri and Bonadonna (2016). In their work the authors show that for a given particle Reynolds number the drag of non-spherical particles is generally higher than an equivalent sphere. Therefore, non-spherical clasts are expected to have lower terminal velocities and longer sedimentation distances along the downwind and crosswind axes with respect to spheres. However, an exhaustive discussion on the role of particle shape on the

computation of isopleth contours is outside the aim of the present work. A brief example of the effects of different values of flatness and elongation is discussed in Appendix A.

Finally, the new theoretical framework has been implemented as a Matlab package (available on request). The user can visualise the envelopes, the sedimentation paths, and isopleth contours. The input parameters are the initial eruptive conditions and the number of particles of a selected released size. The downwind and crosswind distances used for the compilation of nomograms are determined from the modelled isopleth contours. CS86 is prevalently used to invert the plume height based on crosswind and downwind distances. However, the model can have multiple applications. As an example, a forward use of the model allows for the compilation of probability maps required in hazard assessments (e.g. Osman et al. 2018).

4.2. Using the nomograms

Isopleth maps are compiled based on the distribution of the largest clasts observed at various distances from the vent. The two most common statistical strategies used to characterize the largest clasts are the average of the five largest clasts and the median value of a given population (e.g. Bonadonna et al. 2013). Osman et al. (2018) have shown that modelled isopleth contours as those presented here and in CS86 can be better compared with the arithmetic average of the geometric mean of the three axes of the five largest clasts. In addition, the collection of sub-spherical clasts is recommended for the application of standard nomograms, as they have been compiled based on the assumption of spheres. We present nomograms for a temperate climate zone, six densities, and three eruptive scenarios. However, eruptions may occur at almost any latitude and the characteristics of the clasts may not coincide with those considered in the nomograms. In the Supplementary Material, we show how the application of nomograms of Figures 8 and 9 to different latitudes can bring up to 20% additional error in the estimation of height. For higher accuracy, it is recommended to apply the provided Matlab package to specify more accurate topography, meteorological profiles, particle density and particle shape.

4.3. Caveats

The main caveats of the presented model need to be discussed in order to assure a correct application of the proposed methodology. First, the assumption that the effects of the atmospheric winds on the umbrella cloud are negligible compared to the gravity current leads to an overestimation of the upwind axis of the isopleth contours and an underestimation of the downwind distance. This approximation holds for large eruptions, where the velocity of the radial spreading is higher, but it is not necessarily verified for small ones (i.e. plume height <

10 km). However, the role of the gravity current on the sedimentation process with respect to the role of wind in the free atmosphere becomes less important as the plume height h_p decreases, given that the thickness of gravity current scales as $h_{gc} \sim 0.3\, h_p$ (Bonadonna and Phillips 2003). Second, the value of the wind V_{wind} in Eq. (2) (taken at the central axis of the plume) is assumed to depend only on the height z and not on the radial coordinate r. We can quantify the error that this assumption brings into Eq. (4). For a linear expansion of wind around its value along the central axis ($V_{wind} \approx c_1 \times r + c_0$), our approximation neglects the term $K_1 = \frac{2}{3} c_1 \times \cos(\theta) \times R$ in Eq.4. For example, if we consider a typical wind profile as in CS86, the relative importance of the variation of wind velocity along the radial axis can be quantified as $\approx \frac{R\cos(\theta)}{z}$. From this relationship, it follows that our approximation is exact when $\theta \approx 90^\circ$ (strong plumes and the initial part of weak plumes). However, by definition, weak plumes are characterized by lower exit velocity at the vent, a reduced radial entrainment and thus a slower increase of the radius respect to strong plumes for a fixed height. This produces $\frac{R}{z} < 1$ in most parts of the volcanic column for a weak plume, as also confirmed by the simulations with the one-dimensional plume model. We can thus deduce that our approximation holds for most part of the column, except for the upper part of weak plumes.

Finally, the drag formula of Bagheri and Bonadonna (2016) is derived under the assumption of laminar conditions in the upstream flow. We found that its application in a turbulent environment, i.e. inside the plume region, leads to an underestimation of the final maximum sedimentation distances of about 5% for low intensity scenarios, 3% for intermediate and less than 1% for large ones.

5. Conclusions

The present work introduces a new versatile and comprehensive methodology to determine plume height and wind speed from the distribution of the largest clasts around the volcano. The original approach of CS86 has been revised, generalised and modified to include important aspects of plume dynamics and particle sedimentation:

1) A more detailed description of the contribution of wind advection on the shape of the clast support envelope.

2) A new parameterization of the radial spreading of the umbrella cloud to avoid unrealistic velocities for distances smaller than the plume radius (which is where clast support envelopes are constructed).
3) The effect of the atmospheric structure at different latitudes on plume dynamics.
4) The effect of particle shape on particle sedimentation (clasts are described in terms of their flatness and elongation).
5) Three-dimensional ECMWF meteorological fields for eruptions after 1979.
6) Three-dimensional topography that allows for accurate isopleth contours to be compiled.
7) Quantification of the uncertainties related to the use of the nomograms.

For complex eruptive and atmospheric conditions, the reader is recommended to apply the provided Matlab package (available on request) to determine the plume height. However, for an easy application of the strategy, a set of 6 nomograms for three eruptive scenarios (low, intermediate and high intensity scenarios), 2 particle sizes (1.6 and 3.2 mm), density of 2500 kg/m^3, temperate latitude and spherical particle shape is provided (equivalent nomograms for 0.8 and 6.4 cm clasts are provided in the *Supplementary Materials* and a Matlab script is also downloadable from the journal website). A set of aerodynamical equivalent sizes are also indicated for densities between 250-2500 kg/m^3. Discrepancies associated with tropical and arctic latitudes (between 7-20%) are also discussed in *Supplementary Material S6*.

Based on our analysis, we can conclude that:

1) Wind advection on plume rise results in bent clast-support envelopes, and, therefore, in a non-linear relationship between plume height and particle sedimentation, which requires the introduction of three eruptive scenarios for the compilation of nomograms (based on mass flow rate).
2) Due to the effect of bent columns, heights of weak plumes estimated with the new nomograms are generally lower than those calculated with CS86.
3) The effect of particle shape on particle sedimentation results in downwind distances 36 to 70% larger than the equivalent spheres for the test case under analysis (i.e. MSH).
4) The effect of atmospheric structure at different latitudes on plume dynamics is more significant for weak and transitional plumes than for strong plumes; discrepancies between plume height estimates at tropical and arctic latitudes with respect to temperate latitudes are between 7% and 20%.

Acknowledgments

The research leading to these results has received funding from the European Union Seventh Framework Programme (FP7/2007-2013) under the project NEMOH, grant agreement n° 289976. The authors are grateful to Sebastien Biass for his help in handling meteorological data. L. Mastin and D. Jessop are also thanked for their thorough review that largely improved the manuscript and T. Mather for her constructive editorial work.

Appendix A – Effects of clast shape on the computation of isopleth contours

The nomograms of section 2.6 are evaluated assuming spherical particles. However, the Matlab package associated with this study allows the use of non-spherical shapes in the evaluation of terminal velocities and thus in the final isopleth lines. The aim of this appendix is to provide an example of the influence of clast shapes on the downwind and crosswind ranges. We adopted the drag coefficient for irregular particles provided by Bagheri and Bonadonna (2016) that takes into account the effect of flatness and elongation on the drag.

The form factors *flatness fl* and *elongation el* are expressed as a function of the longest (L), the intermediate (I) and the shortest (S) length of the particle ($fl = \frac{S}{I};\ el = \frac{I}{L}$). These three parameters can be measured with the low operator-dependent error following the so-called *projection area protocol* (Bagheri et al., 2015).

The drag coefficient C_d is expressed as:

$$C_d = \frac{24}{Re_p}\, k_S \left(1 + 0.125 \cdot \left(Re_p \frac{k_N}{k_S}\right)^{2/3}\right) + \frac{0.46\, k_N}{1 + 5330/(Re_p \cdot k_N/k_S)} \qquad \text{(Eq.A.1)}$$

The drag coefficient is a function of the particle Reynolds number Re_p and two numbers associated with the shape of the objects: the Newton's drag correction $k_N = 10^{[0.45 \cdot (-\log(F_N)^{0.99})]}$ and the Stokes' drag correction $k_S = \frac{1}{2}\left(F_S^{1/3} + F_S^{-1/3}\right)$. We use simplified expressions to relate F_S and F_N with the flatness and elongation of the particle. Using Table 8 in Bagheri and Bonadonna (2016), we have $F_S = fl \cdot el^{1.3}$ and $F_N = fl^2 \cdot el$.

The fact that the terminal velocity appears both on the left-hand side and on the right-hand side of (Eq. 6) requires an iterative procedure to obtain the solution. As an example, we discuss the application to the tephra deposit associated with the 1980 eruption of Mt St Helens. Initial parameters are fixed and selected from one of the combinations reported in Table (S1) (see *supplementary materials*). We consider particles with a geometric diameter of 1 cm and four different shapes: spherical ($fl = el = 1$), disk-like ($fl = 0.1; el = 1$), needle-like ($fl = 1; el = 0.1$) and intermediate ($fl = el = 0.5$). According to Fig. A.1, the sedimentation of non-spherical particles results in larger downwind and crosswind ranges with respect to the sedimentation of spherical particles. In particular, needle-like and disk-like shapes can have downwind distances that are 36% and 70% larger than those of spheres, respectively. Given

584 that, for simplicity, nomograms can only be constructed based on the spherical assumptions,
585 particular attention should be given when applied to very irregular clasts. As a rule of thumb,
586 the flatter the clast the larger the distance travelled, and plume height could be underestimated.
587 For best results in the determination of plume height, we recommend collecting sub-spherical
588 clasts for the compilation of isopleth maps (e.g. Bonadonna et al. 2013). Alternatively, in case
589 most available clasts are irregular, the direct use of the provided Matlab package is
590 recommended (where particle flatness and elongation can be specified).
591
592

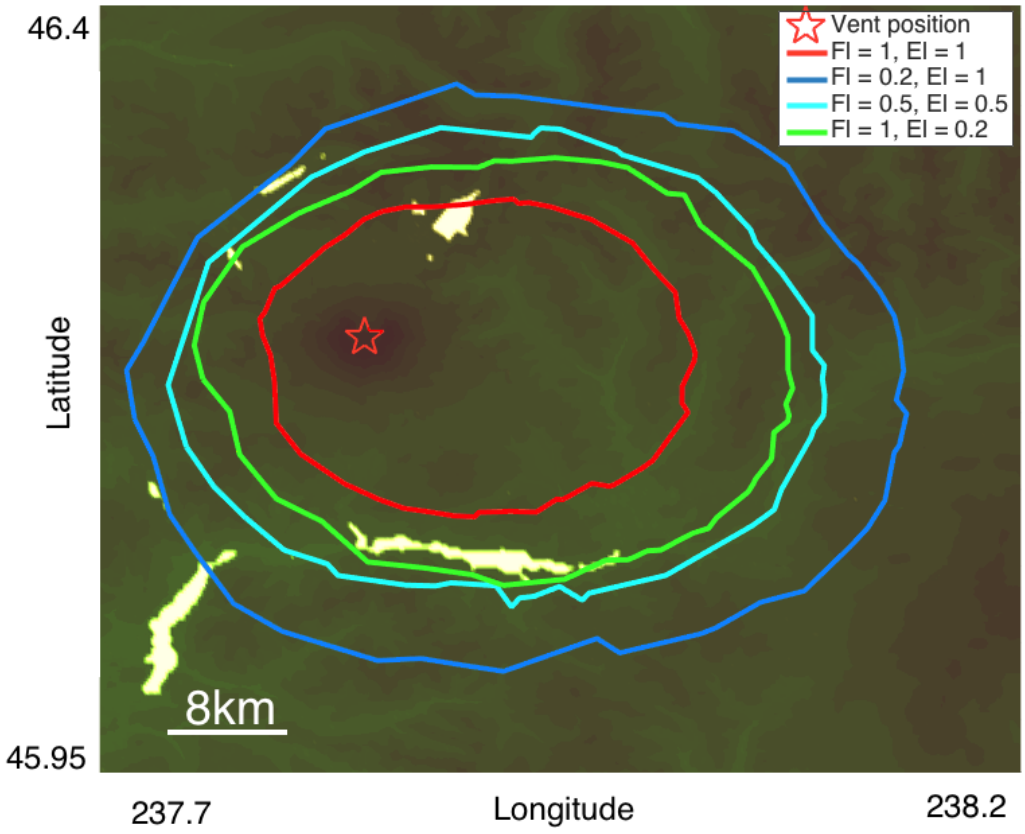

593
594

595 **Figure A.1** Effect of particle shape on the sedimentation distances for lithics with a diameter of 1
596 cm for the eruption of Mount Saint-Helens 1980. Four different shapes are investigated: spheres
597 ($\boldsymbol{fl}$ = $\boldsymbol{el}$ =1), disk-like ($\boldsymbol{fl}$ =0.1; $\boldsymbol{el}$ =1), needle-like ($\boldsymbol{fl}$ =1, $\boldsymbol{el}$ =0.1) and intermediate ($\boldsymbol{fl}$ = $\boldsymbol{el}$ =0.5).

598

References

Bagheri, G. and Bonadonna, C., 2016. On the drag of freely falling non-spherical particles. Powder Technol., 301: 526-544.

Bagheri, G.H., Bonadonna, C., Manzella, I. and Vonlanthen, P., 2015. On the characterization of size and shape of irregular particles. Powder Technol., 270: 141-153.

Biass, S., Bonadonna, C., Connor, L. and Connor, C., 2016. TephraProb: a Matlab package for probabilistic hazard assessments of tephra fallout. Journal of Applied Volcanology, 5(1): 10.

Bonadonna, C. and Costa, A., 2012. Estimating the volume of tephra deposits: A new simple strategy. Geology, 40(5): 415-418.

Bonadonna, C. and Houghton, B.F., 2005. Total grain-size distribution and volume of tephra-fall deposits. Bulletin of Volcanology, 67(5): 441-456.

Bonadonna, C. and Phillips, J.C., 2003. Sedimentation from strong volcanic plumes. J. Geophys. Res.-Solid Earth, 108(B7): 28.

Bonadonna, C., Pistolesi, M., Cioni, R., Degruyter, W., Elissondo, M. and Baumann, V., 2015. Dynamics of wind-affected volcanic plumes: The example of the 2011 Cordon Caulle eruption, Chile. J. Geophys. Res.-Solid Earth, 120(4): 2242-2261.

Burden, R.E., Chen, L. and Phillips, J.C., 2013. A statistical method for determining the volume of volcanic fall deposits. Bulletin of Volcanology, 75(6): 10.

Burden, R.E., Phillips, J.C. and Hincks, T.K., 2011. Estimating volcanic plume heights from depositional clast size. J. Geophys. Res.-Solid Earth, 116: 13.

Bursik, M., 2001. Effect of wind on the rise height of volcanic plumes. Geophysical Research Letters, 28(18): 3621-3624.

Carey, S., Sigurdsson, H., Gardner, J.E. and Criswell, W., 1990. Variations in column height and magma discharge during the may 18, 1980, eruption of Moun St. Helens. J. Volcanol. Geotherm. Res., 43(1-4): 99-112.

Carey, S. and Sparks, R.S.J., 1986. Quantitative models of the fallout and dispersal of tephra from volcanic eruption columns. Bulletin of Volcanology, 48(2-3): 109-125.

Castruccio, A., Clavero, J., Segura, A., Samaniego, P., Roche, O., Le Pennec, J.L., Droguett, B., 2016. Eruptive parameters and dynamics of the April 2015 sub-Plinian eruptions of Calbuco volcano (southern Chile). Bulletin of Volcanology 78, 19.

Champion K. S. W., C.A.E., Kantor A. J., 1985. Standard and reference atmospheres. Handbook of geophysics and the space environment.

Costa, A., Folch, A. and Macedonio, G., 2013. Density-driven transport in the umbrella region of volcanic clouds: Implications for tephra dispersion models. Geophysical Research Letters, 40(18): 4823-4827.

Costa, A., Suzuki, Y.J., Cerminara, M., Devenish, B.J., Ongaro, T.E., Herzog, M., Van Eaton, A.R., Denby, L.C., Bursik, M., Vitturi, M.D., Engwell, S., Neri, A., Barsotti, S., Folch, A., Macedonio, G., Girault, F., Carazzo, G., Tait, S., Kaminski, E., Mastin, L.G., Woodhouse, M.J., Phillips, J.C., Hogg, A.J., Degruyter, W., Bonadonna, C., 2016. Results of the eruptive column model inter-comparison study. J. Volcanol. Geotherm. Res. 326, 2-25

Davidson, G.A., 1986. Gaussian versus top-hat profile assumptions in integral plume models. Atmospheric Environment, 20(3): 471-478.

De' Michieli Vitturi, M., Neri, A., Ongaro, T.E., Lo Savio, S. and Boschi, E., 2010. Lagrangian modeling of large volcanic particles: Application to Vulcanian explosions. J. Geophys. Res.-Solid Earth, 115: 18.

Dee, D.P., Uppala, S.M., Simmons, A.J., Berrisford, P., Poli, P., Kobayashi, S., Andrae, U., Balmaseda, M.A., Balsamo, G., Bauer, P., Bechtold, P., Beljaars, A.C.M., van de Berg, L., Bidlot, J., Bormann, N., Delsol, C., Dragani, R., Fuentes, M., Geer, A.J.,

649 Haimberger, L., Healy, S.B., Hersbach, H., Holm, E.V., Isaksen, L., Kallberg, P.,
650 Kohler, M., Matricardi, M., McNally, A.P., Monge-Sanz, B.M., Morcrette, J.J., Park,
651 B.K., Peubey, C., de Rosnay, P., Tavolato, C., Thepaut, J.N. and Vitart, F., 2011. The
652 ERA-Interim reanalysis: configuration and performance of the data assimilation system.
653 Q. J. R. Meteorol. Soc., 137(656): 553-597.
654 Degruyter, W. and Bonadonna, C., 2012. Improving on mass flow rate estimates of volcanic
655 eruptions. Geophysical Research Letters, 39(16): n/a-n/a.
656 Degruyter, W. and Bonadonna, C., 2013. Impact of wind on the condition for column collapse
657 of volcanic plumes. Earth and Planetary Science Letters, 377-378: 218-226.
658 Devenish, B.J., Rooney, G.G., Webster, H.N. and Thomson, D.J., 2010. The Entrainment Rate
659 for Buoyant Plumes in a Crossflow. Bound.-Layer Meteor., 134(3): 411-439.
660 Fierstein, J. and Nathenson, M., 1992. Another look at the calculation of fallout tephra volumes.
661 Bulletin of Volcanology, 54(2): 156-167.
662 Folch, A., Costa, A., Macedonio, G., 2016. FPLUME-1.0: An integral volcanic plume model
663 accounting for ash aggregation. Geoscientific Model Development 9, 431-450.
664 Ganser, G.H., 1993. A rational approach to drag prediction of spherical and nonspherical
665 particles. Powder Technol., 77(2): 143-152.
666 Glaze, L.S., Baloga, S.M., Wilson, L., 1997. Transport of atmospheric water vapor by volcanic
667 eruption columns. J. Geophys. Res.-Atmos. 102, 6099-6108.
668 Haider, A. and Levenspiel, O., 1989. Drag coefficient and terminal velocity of spherical and
669 nonspherical particles. Powder Technol., 58(1): 63-70.
670 Holasek, R.E., Self, S., 1995. GOES weather-satellite observations and measurements of the
671 May 18, 1980, Mount-St-Helens eruption. J. Geophys. Res.-Solid Earth 100, 8469-
672 8487.
673 Holasek, R.E., Self, S. and Woods, A.W., 1996. Satellite observations and interpretation of the
674 1991 Mount Pinatubo eruption plumes. J. Geophys. Res.-Solid Earth, 101(B12): 27635-
675 27655.
676 Hoult, D.P., Weil, J.C., 1972. Turbulent plume in a laminar cross flow. Atmospheric
677 Environment 6, 513
678 Jessop, D.E., Jellinek, A.M., 2014. Effects of particle mixtures and nozzle geometry on
679 entrainment into volcanic jets. Geophysical Research Letters 41, 3858-3863.
680 Johnson, C.G., Hogg, A.J., Huppert, H.E., Sparks, R.S.J., Phillips, J.C., Slim, A.C.,
681 Woodhouse, M.J., 2015. Modelling intrusions through quiescent and moving ambients.
682 J. Fluid Mech. 771, 37.
683 Maeno, F., Nagai, M., Nakada, S., Burden, R.E., Engwell, S., Suzuki, Y. and Kaneko, T., 2014.
684 Constraining tephra dispersion and deposition from three subplinian explosions in 2011
685 at Shinmoedake volcano, Kyushu, Japan. Bulletin of Volcanology, 76(6): 16.
686 Nathenson, M., 2017. Revised tephra volumes for Cascade Range volcanoes. J. Volcanol.
687 Geotherm. Res., 341: 42-52.
688 Osman, S., Rossi, E., Bonadonna, C., Frischknecht, C., Andronico, D., Cioni, R., and Scollo,
689 S.(in review, 2018) Exposure-based risk assessment and emergency management
690 associated with the fallout of large clasts, Nat. Hazards Earth Syst. Sci. Discuss.,
691 https://doi.org/10.5194/nhess-2018-91
692 Patrick, M.R., 2007. Dynamics of Strombolian ash plumes from thermal video: Motion,
693 morphology, and air entrainment. Journal o Geophysical Research, 112(B6).
694 Pouget, S., Bursik, M., Webley, P., Dehn, J. and Pavolonis, M., 2013. Estimation of eruption
695 source parameters from umbrella cloud or downwind plume growth rate. J. Volcanol.
696 Geotherm. Res., 258: 100-112.
697 Pyle, D.M., 1989. The thickness, volume and grainsize of tephra fall deposits. Bulletin of
698 Volcanology, 51(1): 1-15.

699 Rosi, M., Paladio-Melosantos, M.L., Di Muro, A., Leoni, R. and Bacolcol, T., 2001. Fall vs
700 flow activity during the 1991 climactic eruption of Pinatubo Volcano (Philippines).
701 Bulletin of Volcanology, 62(8): 549-566.
702 Shampine, L.F. and Reichelt, M.W., 1997. The MATLAB ODE suite. SIAM J. Sci. Comput.,
703 18(1): 1-22.
704 Shapiro, M.A., Hampel, T. and Krueger, A.J., 1987. The arctic tropopause fold. Mon. Weather
705 Rev., 115(2): 444-454.
706 Sparks, R.S.J., 1986. The dimensions and dynamics of volcanic eruption columns. Bulletin of
707 volcanology, 48: 3-15.
708 Sparks, R.S.J. and Wilson, L., 1982. Explosive volcanic-eruptions. 5. Observations of plume
709 dynamics during the 1979 Soufriere eruption, St. Vincent. Geophysical Journal of the
710 Royal Astronomical Society, 69(2): 551-570.
711 Stull, R.B., 2005. Meteorology For Scientists And Engineers. Brooks/Cole.
712 Sulpizio, R., 2005. Three empirical methods for the calculation of distal volume of tephra-fall
713 deposits. J. Volcanol. Geotherm. Res., 145(3-4): 315-336.
714 Suzuki, Y.J. and Koyaguchi, T., 2013. 3D numerical simulation of volcanic eruption clouds
715 during the 2011 Shinmoe-dake eruptions. Earth Planets Space, 65(6): 581-589.
716 Woodhouse, M.J., Hogg, A.J., Phillips, J.C. and Sparks, R.S.J., 2013. Interaction between
717 volcanic plumes and wind during the 2010 Eyjafjallajökull eruption, Iceland. Journal of
718 Geophysical Research: Solid Earth, 118(1): 92-109.
719 Woods, A.W., 1988. The fluid-dynamics and thermodynamics of eruption columns. Bulletin of
720 Volcanology, 50(3): 169-193.
721
722

Figures

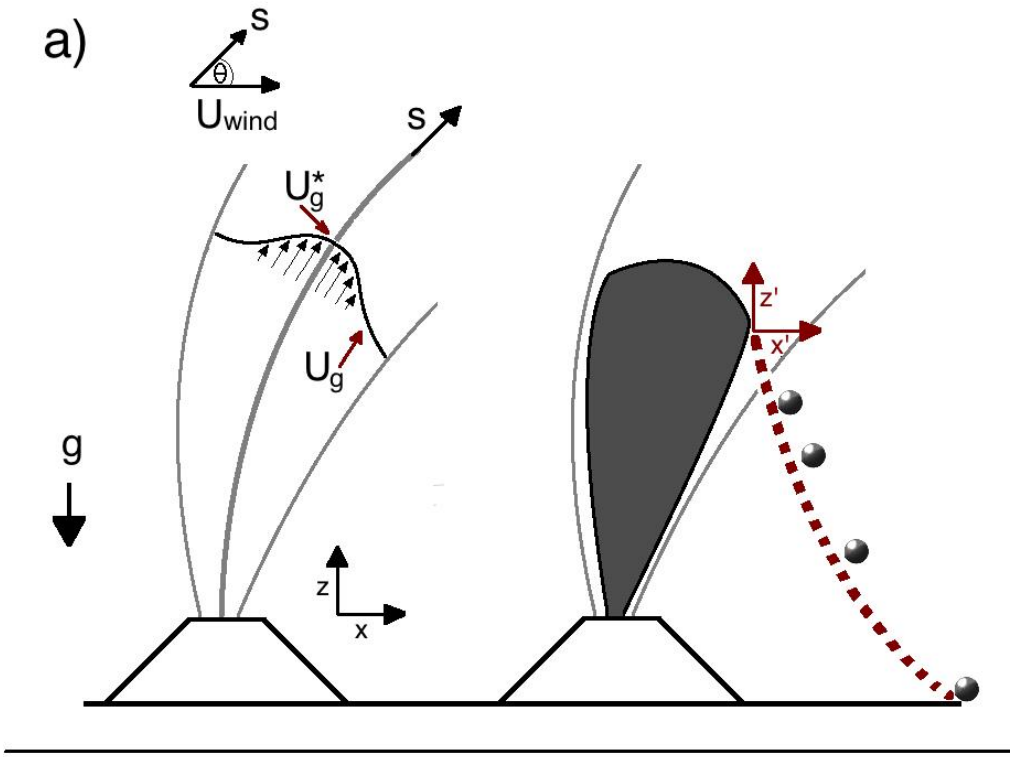

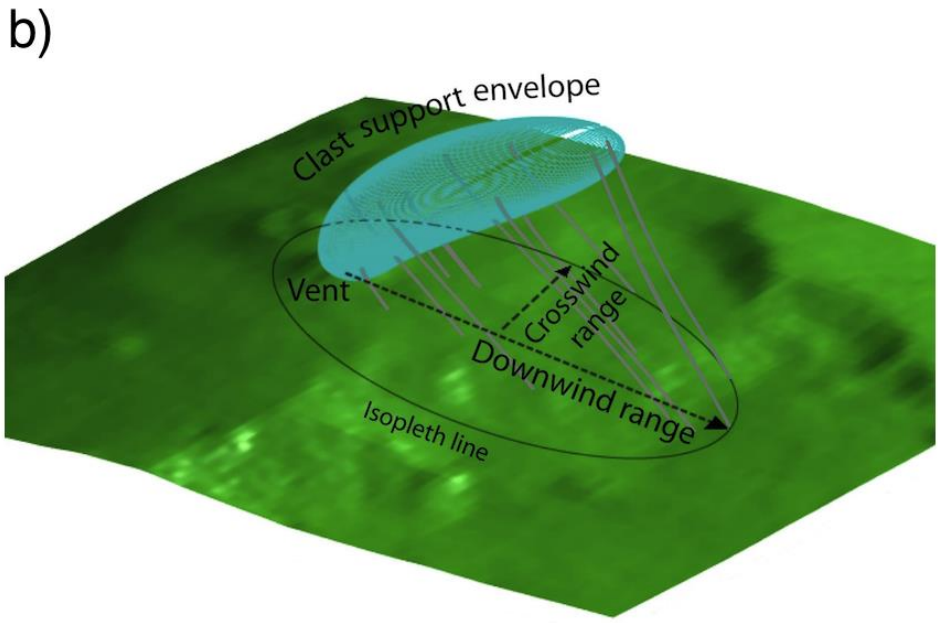

Figure 1 (a) Diagram of the coordinate system used to describe plume rise and particle sedimentation from the clast support envelope, shown in grey shaded colour; (b) Example of clast support envelope produced by the model with particle trajectories in the atmosphere and definition of downwind and crosswind range following CS86.

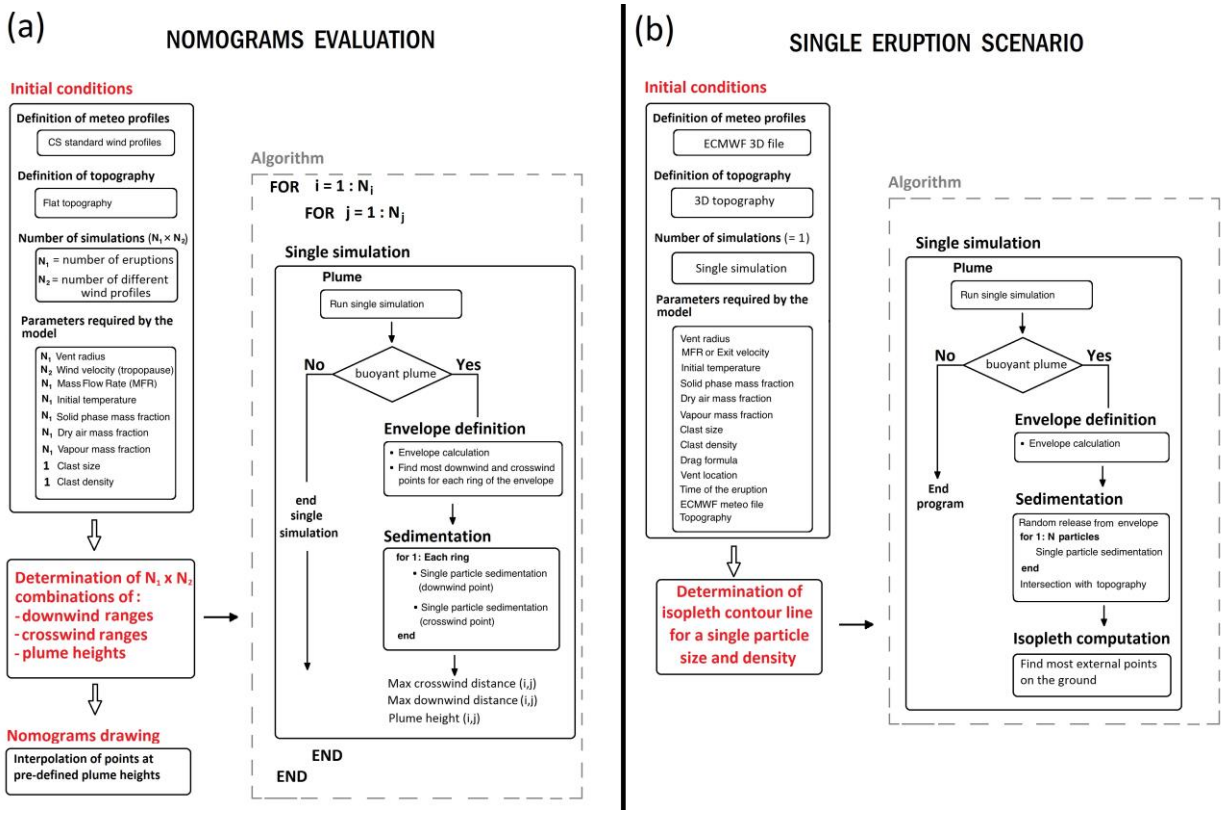

Figure 2 Flowchart of the two main applications of the model: (a) Compilation of nomograms: this approach is used to compile the nomograms: the model is run several times in a Montecarlo approach varying the initial eruptive conditions and the maximum wind at the tropopause. The final set of points relates the height of the plume with the maximum downwind and crosswind ranges obtained in each simulation. Nomograms are derived by interpolating the information at pre-defined plume heights (i.e. 5, 10, 15, 20, 25, 30 km). (b) The second approach allows the user to run single simulations with complete topography and three dimensional meteorological data. The final result is the computation of the isopleth map for a given particle size and density.

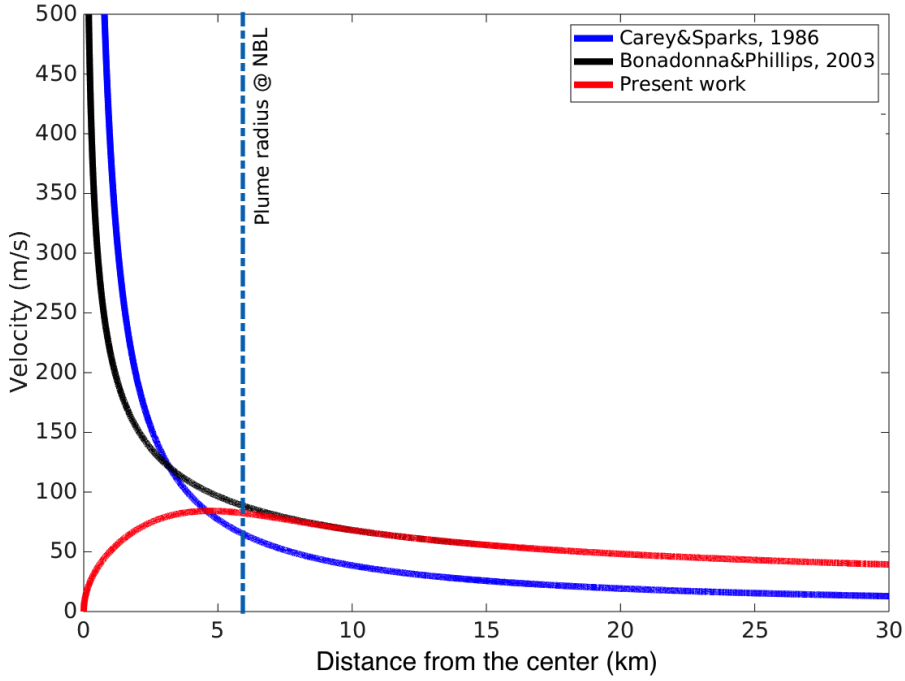

Figure 3 Velocity of the gravity current as a function of the distance from the center of the umbrella cloud, according to CS86, Bonadonna and Phillips (2003) and the present work (Eq. (11)). Outside the NBL the parameterization of Bonadonna and Phillips (2003) and our model are the same, with the exception of an initial 7% of difference in correspondence of the NBL. The formula proposed in the present work avoids the mathematical singularity for a null distance.

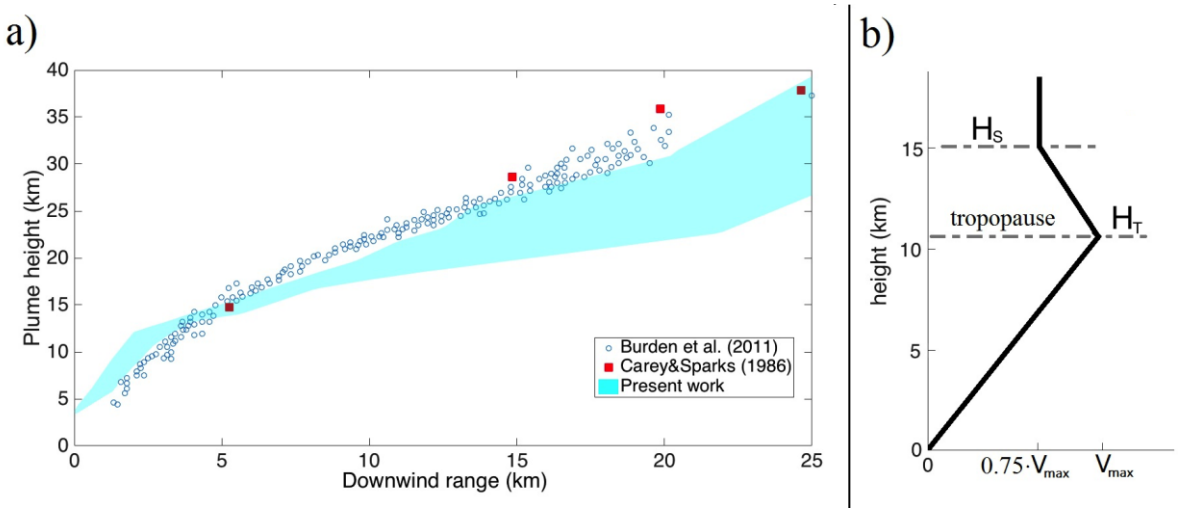

Figure 4 Comparison of our model with the models of CS86 and BPH11 for the same initial eruptive conditions and a no wind case. Initial conditions are the same of table 1 in BPH11. Red dots are points extrapolated from the nomograms of CS86, while the blue circles represent data of BPH11; the shadowed area in the plot describes the space of possible outcomes according to the present model. Particle size is 0.8 cm and particle density is 2500 kg/m^3. (b) Typical wind profile used in the nomograms. H_T is the height of the tropopause and H_S is the height at which the wind profile is constant. V_{max} defines the maximum value of the wind at the tropopause.

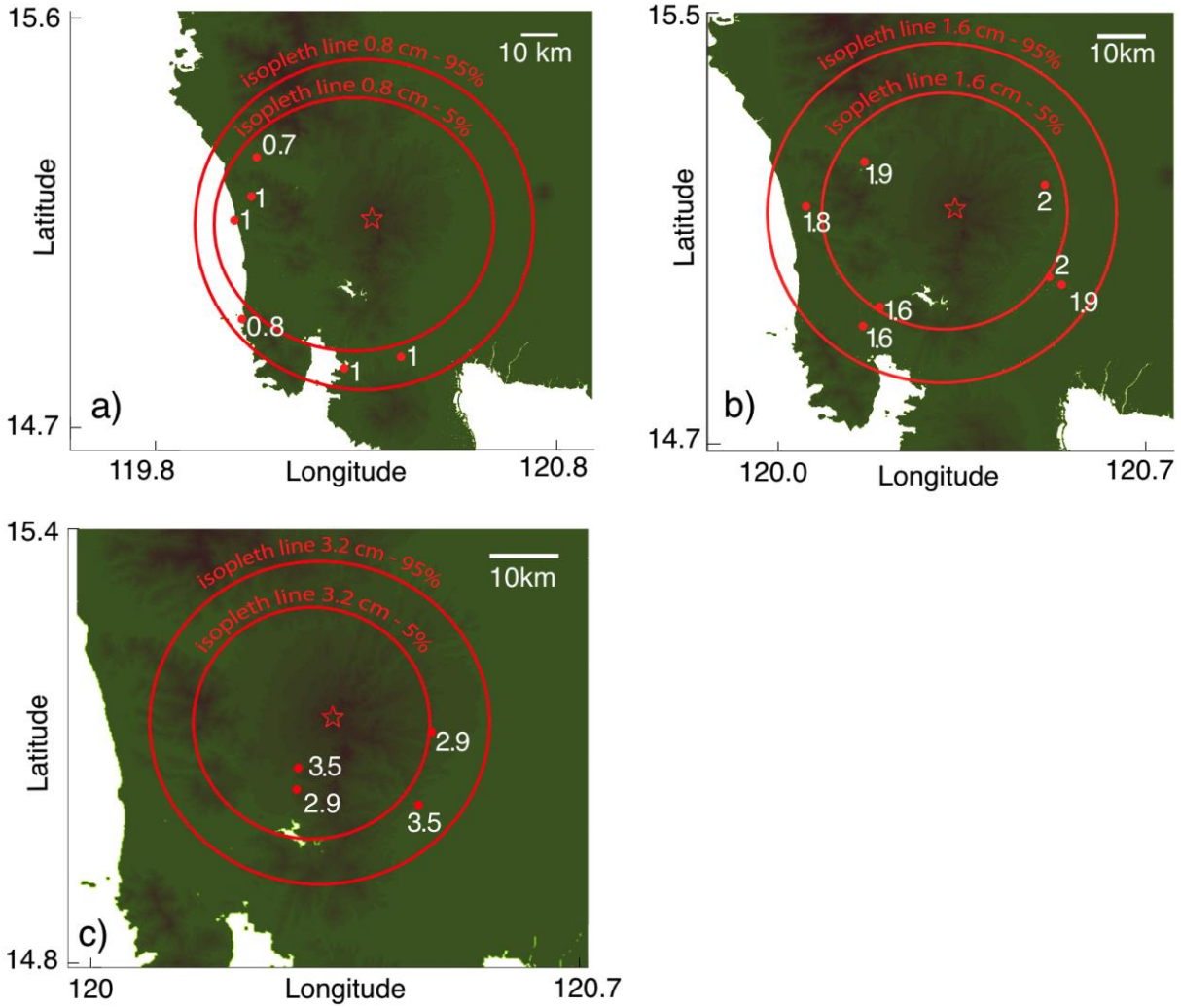

Figure 5 Mount Pinatubo, 1991: comparison of field data points (in cm; red dots) with computed isopleth contours (red lines) with confidence levels of 5% and 95%. Isopleth contours are computed for the following lithic sizes: a) 0.8 cm b) 1.6 cm c) 3.2 cm.

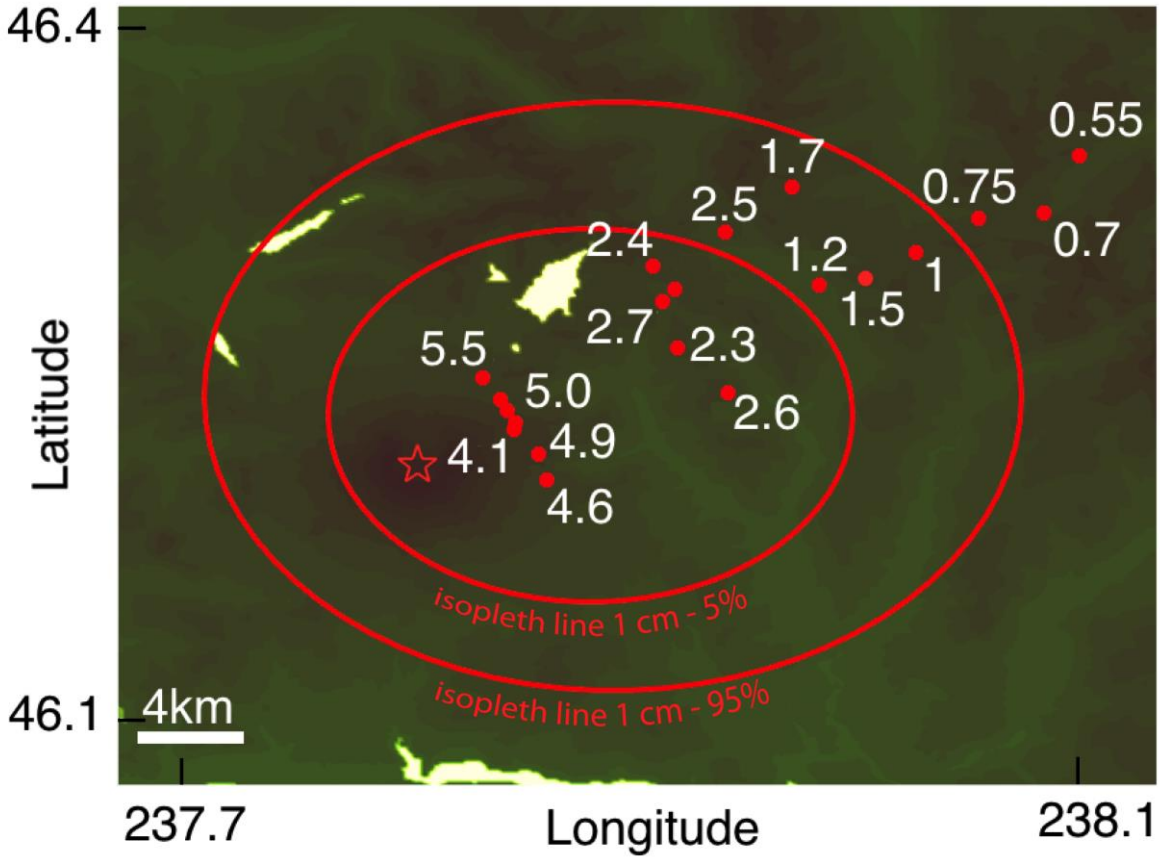

761

762 **Figure 6** Mount Saint Helens, 1980: comparison of field data points from the B2 phase (in cm; red dots)
763 with computed isopleth contours (red lines) with confidence levels of 5% and 95%. Isopleth lines are
764 computed for lithics with 1 cm of diameter.

765

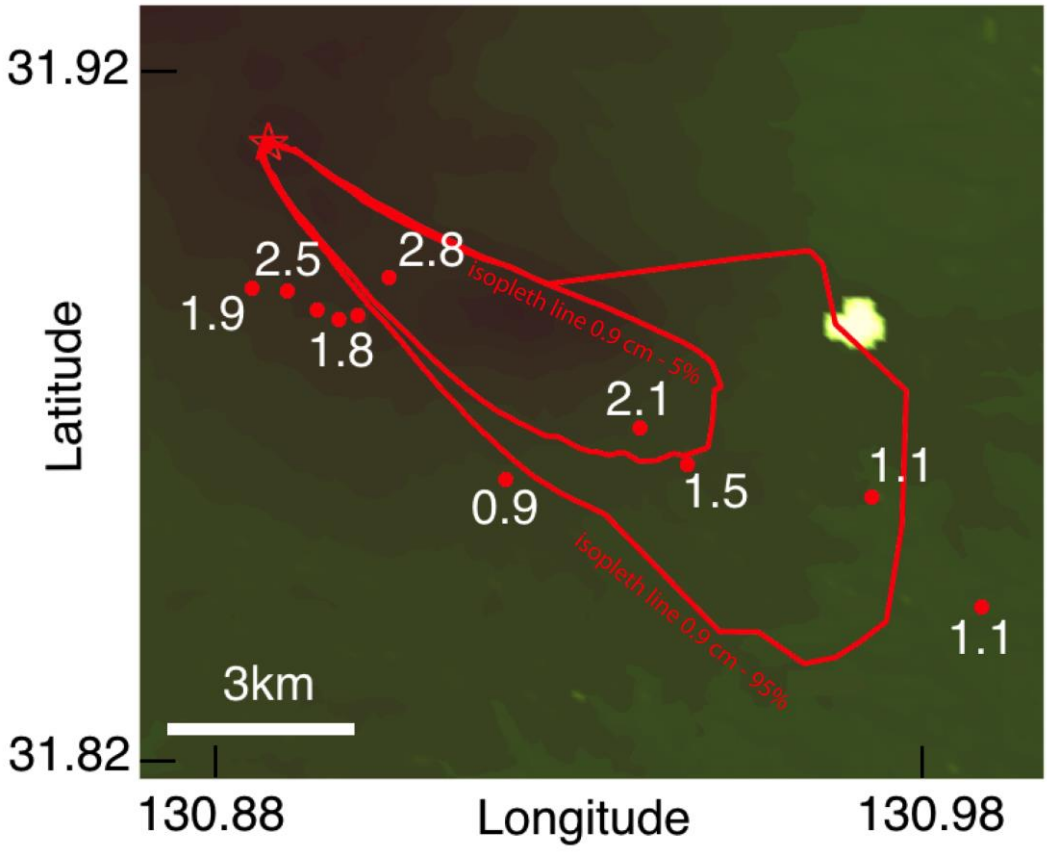

766

767 **Figure 7** Shinmoedake, 2011: comparison of field data points for the three eruptions of 26th-27th of
768 January 2011 (in cm; red dots) with computed isopleth contours (red lines) with confidence levels of
769 5% and 95%. Isopleth lines are computed for lithics with 0.9 cm diameter.

770

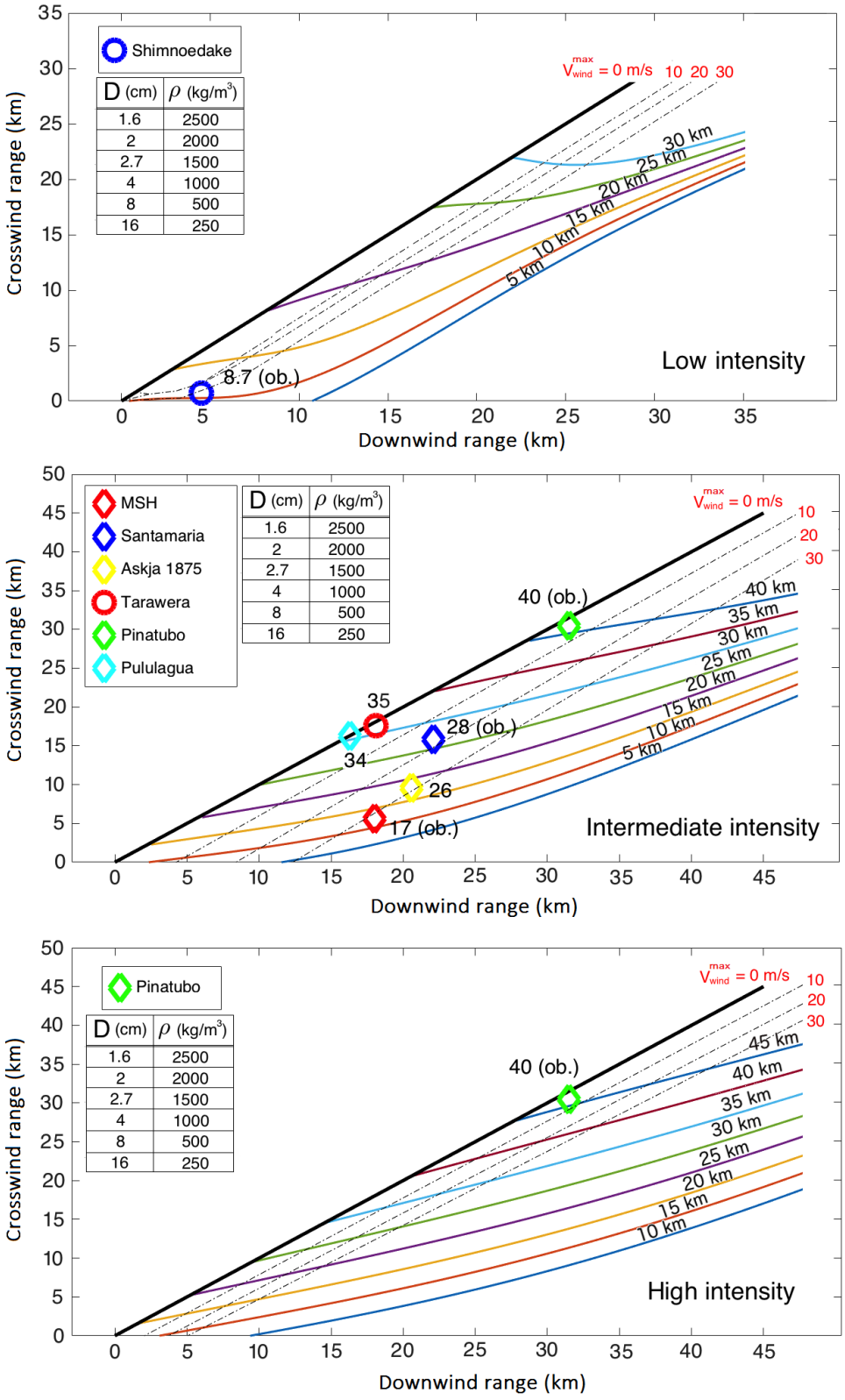

771

772 **Figure** 8 Nomograms for lithics of 1.6 cm of diameter and aerodynamically equivalent combinations of
773 size and densities for 3 eruptive scenarios: low, intermediate and high intensity. Dashed lines represent
774 pairs of points characterized with same values of maximum wind at the tropopause ($\boldsymbol{V_{wind}^{max}}$).

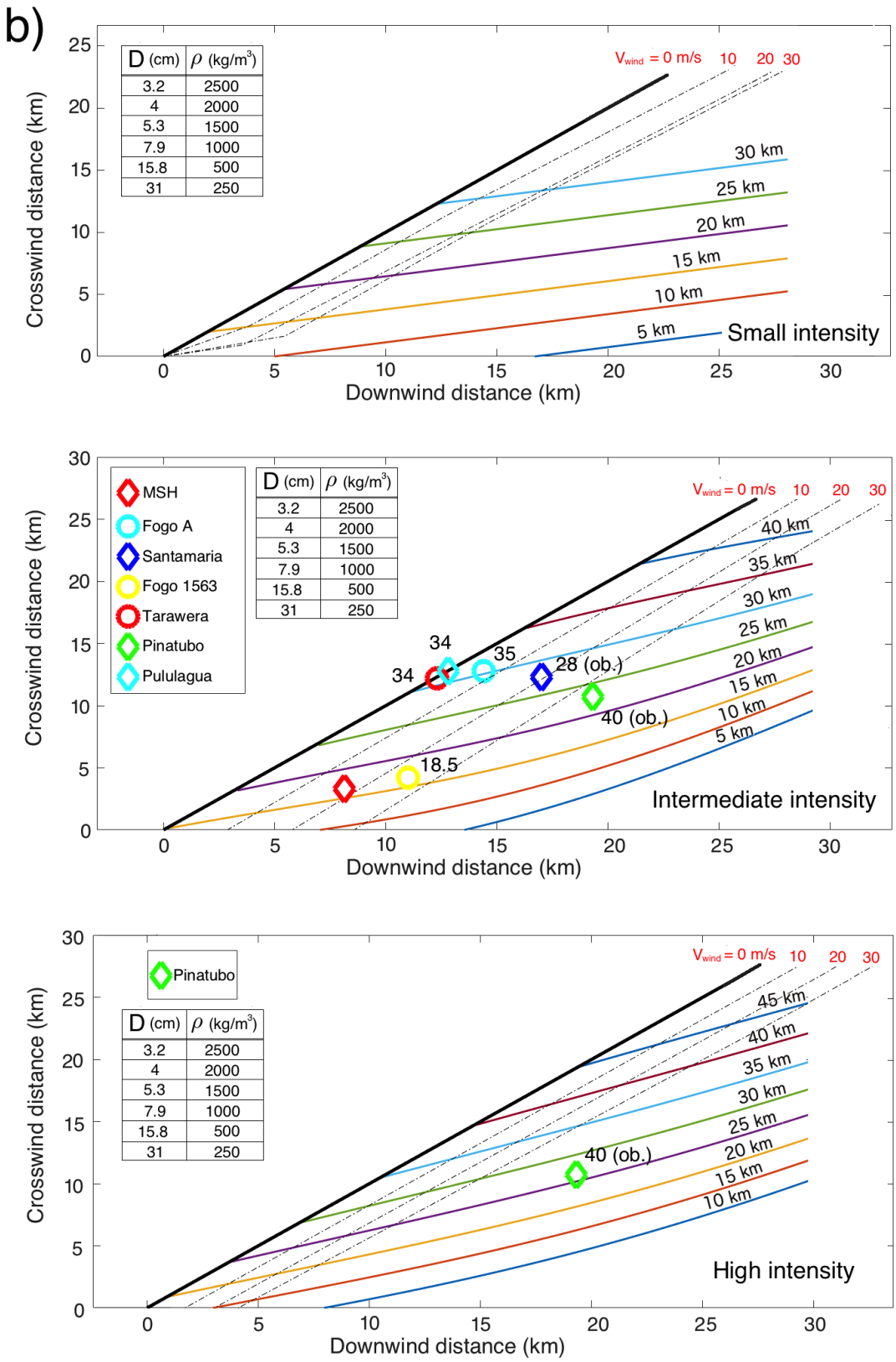

Figure 9 Nomograms for lithics of 3.2 cm of diameter and aerodynamically equivalent combinations of size and densities for 3 eruptive scenarios: low, intermediate and high intensity. Dashed lines represent pairs of points characterized with same values of maximum wind at the tropopause (V_{wind}^{max}).

Tables

Table 1

Comparison between observed plume height and plume height determined using both our new nomograms (Figs 8 and 9) and those of CS86. As described in the text, both the predicted heights (columns 4 and 5) have to be compared with observed plume heights relatively to the sampling altitude (column 3). The values in parenthesis in columns 4 and 5 represent the relative discrepancy with respect to values in column 3. All values in column 5 have been recalculated with CS86 for this work (based on the isopleth contours of 5cm for Calbuco, 1.6cm and 0.8 cm for MSH, 1,6 and 0.8 cm for Pinatubo, 1.6cm, 3.2cm and 6.4 cm for Santamaria and 0.8 and 1.6 cm for Shinmoedake).

Eruption	Observed plume height above the vent (km)	Observed plume height relatively to sampling altitude (km)	Predicted plume height (this work) (km)	Predicted plume height (CS86) (km)
Calbuco 2015	≈15 [(i)]	16.5	17 [(6)] (3.0%)	18 [(6)] (9.1%)
Mount Saint Helens 1980 (B2 phase)	13.5– 15.5 [(2)]	14.5 – 16.5	15[(7)] (3.4% - 9.1%)	19[(7)] (31.0% - 15.2%)
Pinatubo 1991	39 [(3)]	40	37-42 (1.3%)	≈43 (7.5%)
Santamaria 1902	24-26 [(4)]	26-28	27 (0.0%)	34 (25.9%)
Shinmoedake 2011	7.3 [(5)]	8.4	10-11 (25.0%)	8.6 (2.4%)
Askja 1875	NA	NA	17-22	26
Fogo A	NA	NA	30.5	35
Fogo 1563	NA	NA	16	18.5
Pululagua 2450 BP	NA	NA	31	34
Tarawera 1886	NA	NA	30	34

[1] Radar observation, Vidal et al. (2017) (observation related to the 1st plume of Calbuco 2015, i.e. corresponding to Layer 1 of Castruccio et al. (2016)); [2] satellite (left value) and radar (right value) observations relatively to B2 phase, Holasek & Self (1995); [3] satellite observation, Holasek et al. (1996); [4] Visual estimation, Anderson (1908); [5] satellite observation, Maeno et al. (2014); [6] this prediction is based on the isopleth contour of 5 cm scoria clasts with a density of 1350 kg/m^3 (Castruccio et al., 2016; Layer 1) and our nomogram for particles with 5.3 cm and density of 1500 kg/m^3 (the Calbuco 2015 eruption was not reported in the nomograms of Figs 8 and 9 since clast size and density from field data do not perfectly match the combinations available in the plots); [7] plume height calculated using an average of 1.6 cm and 3.2 cm nomograms, both for CS86 and the present work (maximum downwind and crosswind ranges are associated with lithic clasts of the B2 phase; Carey et al. (1990)); NA: not available.

Supplementary material 1:

RANGE OF INITIAL CONDITIONS USED FOR THE COMPARISON

The validation process of the model is based on the comparison between field data and computed isopleth lines. However, the determination of the isopleth lines is strongly influenced by the maximum Mass Flow Rate (MFR) of an eruption. This value depends on the fluctuations that occur during the eruption and thus it can differ from the MFR reported in the literature. Moreover, several additional parameters influence the shape of the clast support envelope and clast sedimentation, such as the initial plume radius, the initial mass fraction of solid particles, plume temperature, the shape of particles. All these values are usually not easily constrained, and a probabilistic approach is preferred in order to study a given eruption. In table S1 we report the range of initial conditions used for the validation of the model. Three eruptions are used in this phase: the 1991 Pinatubo eruption, Philippines; the 1980 Mount St Helens eruption, USA; the 2011 Shinmoedake eruption, Japan.

Table S1 – Range of initial conditions used for the validation of the model.

Eruption	MFR (Kg/s)	Plume temperature (K)	Elongation or Flatness	Particles density (kg/m^3)	Mass fraction solid (%)	Radius (m)	Number of simulations
Pinatubo	0.8-1.2 1e9	1100 - 1400	0.5-1	2600-2700	95-97	200-500	200
Mt St Helens	0.7-1 1e8	1100 - 1400	0.5-1	2600-2700	95-97	50-200	200
Shinmoe-dake	1-4 1e6	1100 - 1400	0.5-1	1100-1300	95-97	25-50	100

Supplementary material 2:

PLUME EQUATIONS

The plume model used in this manuscript to derive the clast support envelope is mostly based on the work of Degruyter and Bonadonna (2012, 2013). The model has been adapted with one minor addition: the introduction of the rotation of the plume in the x-y plane by means of the wind azimuthal angle Φ_a(see Eq. S8, S9) as in Folch et al. (2016). Here we summarise the most important assumptions of the plume model of Degruyter and Bonadonna (2012, 2013).

Physical quantities within the plume column are assumed to have self-similar profiles with a top-hat shape. External air is entrained inside the control volume at a rate that depends on the plume velocity. According to (Bursik, 2001; Hoult and Weil, 1972) the entrained velocity U_{entr} is a function of a coefficient α_e along the axis of the plume and a coefficient β_e along the radial direction.

$$U_{entr} = \alpha_e|U_{th} - V_{wind}\, cos\theta| + \beta_e|V_{wind}\, sin\theta| \quad \text{(Eq.S1)}$$

Where $\alpha_e = 0.1$ and $\beta_e = 0.5$ (Devenish et al., 2010). The total mass flow rate Q_{tot} is formed of three different components: dry air, vapour, solid fraction. It continuously grows due to the entrainment of external air into the volcanic plume. No sedimentation of clasts and formation of ice and liquid water are considered in the mass balance equations (Eq.S2, S3, S4). As in Degruyter and Bonadonna (2012), the wind component along the z-axis is neglected, but it can vary in the x-y plane at different heights.

The governing conservation equations are:

$$\text{Dry air: } \frac{d}{ds}(Q_d) = 2\pi R\, \rho_{atm}^{d} U_{entr} \quad \text{(Eq.S2)}$$

$$\text{Vapour: } \frac{d}{ds}(Q_v) = 2\pi R\, \rho_{atm}^{v} U_{entr} \quad \text{(Eq.S3)}$$

$$\text{Solid: } \frac{d}{ds}(Q_s) = 0 \quad \text{(Eq.S4)}$$

$$\text{Momentum: } \frac{d}{ds}(Q_{tot}\, U_{th}) = \pi R^2 g \sin\theta\, (\rho_a - \rho_b) + 2\pi R\, v_{wind} \cos\theta\, \rho_a v_{entr} \quad \text{(Eq.S5)}$$

$$\text{Angle } \theta\text{: } \frac{d\,\theta}{ds} = \frac{\pi R^2 g \cos\theta\, (\rho_a - \rho_b)\ - 2\pi R\, v_{wind} \sin\theta\, \rho_a v_{entr}}{Q_{tot}\, U_{th}} \quad \text{(Eq.S6)}$$

$$\text{Heat: } \frac{d}{ds}(Q_{tot} c_b T_b) = c_a\, T_a \frac{d}{ds}(Q_a) -\ g \sin\theta\, Q_{tot} \quad \text{(Eq.S7)}$$

$$\text{x} - \text{coordinate: } \frac{d}{ds}(x) = \cos\theta\ \cos\Phi_a \quad \text{(Eq.S8)}$$

$$\text{y} - \text{coordinate: } \frac{d}{ds}(y) = \cos\theta\ \sin\Phi_a \quad \text{(Eq.S9)}$$

$$\text{z} - \text{coordinate: } \frac{d}{ds}(z) = \sin\theta \quad \text{(Eq.S10)}$$

Where $Q_{tot} = Q_d + Q_v + Q_s = \pi R^2\, \rho_{th} U_{th}$, $Q_d = \pi R^2\, \rho_b n_d U_{th}$, $Q_v = \pi R^2\, \rho_b n_v U_{th}$, $Q_s = \pi R^2\, \rho_b n_s U_{th}$ and $Q_a = Q_d + Q_v$. The sum of the three mass fractions equals the unity: $n_d + n_v + n_s = 1$. A bulk-density state equation is required in order to close the system:

$$\rho_b = \left[\frac{n_d + n_v}{\rho_{gas}} + \frac{n_s}{\rho_s}\right]^{-1} \quad \text{(Eq.S11)}$$

The density of the gas phase (i.e. the dry air and vapour) is evaluated from the equation of state for perfect gases:

$$\rho_{gas} = \frac{P_{atm}}{R_g\, T_b} \quad \text{(Eq.S12)}$$

Where R_g is a function of the gas constants of the two distinct phases, R_d and R_v, and their mass fractions n_d and n_v:

$$R_g = \frac{n_v\, R_v}{(n_v + n_d)} + \frac{n_d\, R_d}{(n_v + n_d)} \quad \text{(Eq.S13)}$$

The atmospheric densities for dry air and vapor appear inside the entrained air (Eq. S2, S3). They are evaluated as:

$$\rho_{atm}^{d} = \frac{P_{atm}}{R_v T_{atm}} \cdot \frac{1}{(w_a + \varepsilon)} \quad \text{(Eq.S14)}$$

$$\rho_{atm}^{v} = \frac{P_{atm}}{R_v T_{atm}} \cdot \frac{w_a}{\left(w_a + \frac{R_d}{R_v}\right)} \quad \text{(Eq.S15)}$$

Where w_a is the unsaturated mixing ratio, expressed as a function of the saturated mixing ratio w_s:

$$w_a = r_h \cdot w_s \quad \text{(Eq.S16)}$$

$$w_s = \frac{R_v}{R_d} \cdot \frac{P_{sat}}{P_{atm} - P_{sat}} \quad \text{(Eq.S17)}$$

The saturation vapour pressure P_{sat} can be evaluated as a function of the air temperature using the Tetens' formula (Stull, 2005). The set of Ordinary Differential Equations (ODEs) (Eq. S2- Eq. S10) is solved with an explicit Runge-Kutta scheme of $4^{th} - 5^{th}$ order, once that the external input values are provided, such as the air temperature, humidity and density. Atmospheric variables, such as atmospheric temperature and pressure, are read from external files and interpolated at the vent location. More details on the meteorological data will be given in the next sections, together with the mode of operation for long lasting eruptions.

Supplementary material 3:

NOMOGRAMS FOR CLASTS WITH SIZES OF 0.8 cm AND 6.4 cm

Additional nomograms for clasts with sizes of 0.8 cm and 6.4 cm and equivalent terminal velocities.

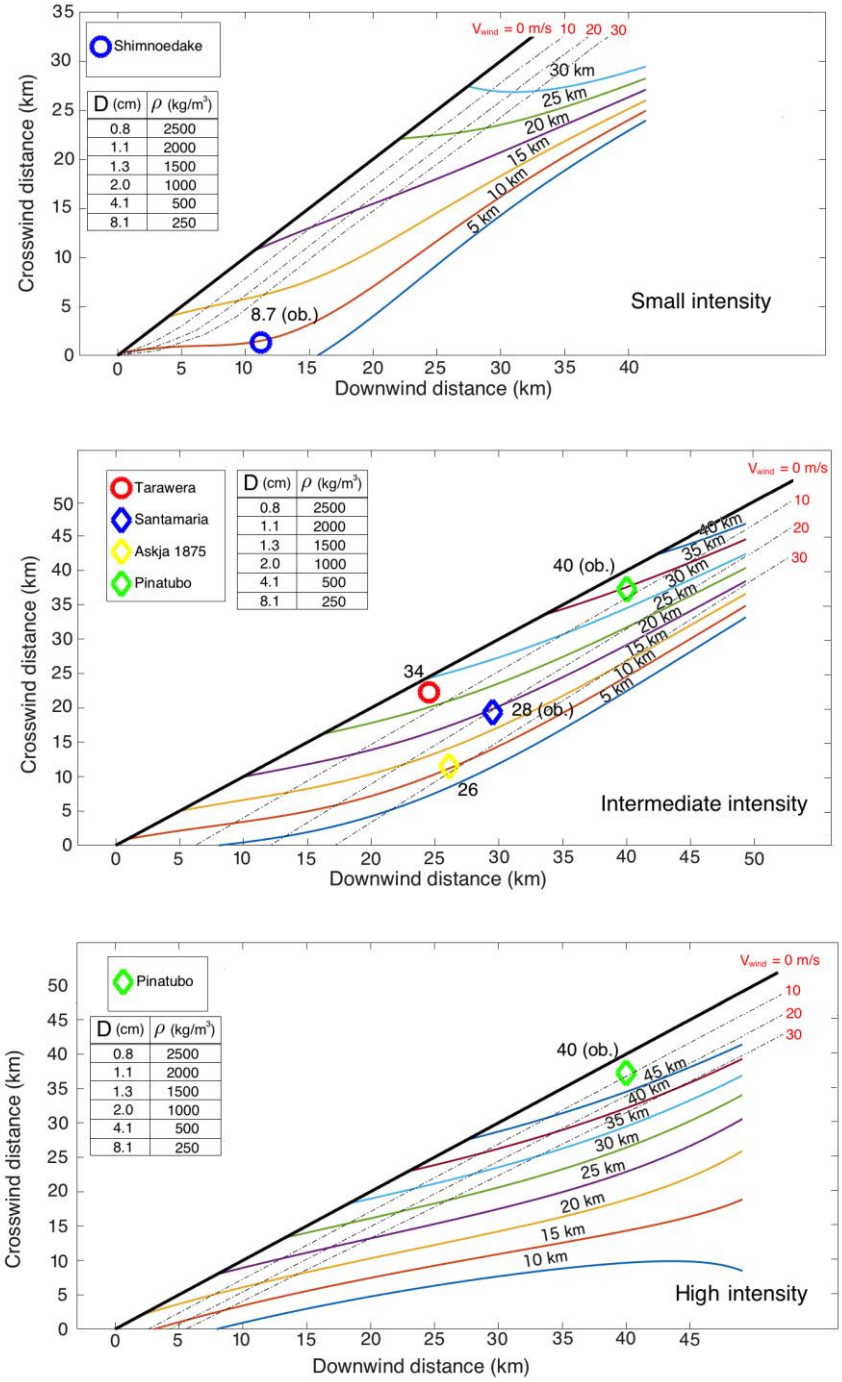

Figure S1: Nomograms for lithics of 0.8 cm of diameter and aerodynamically equivalent combinations of size and densities for 3 eruptive scenarios: low, intermediate and high intensity. Dot-dashed lines represent pairs of points characterized with same values of maximum wind at the tropopause (V_{wind}^{max}).

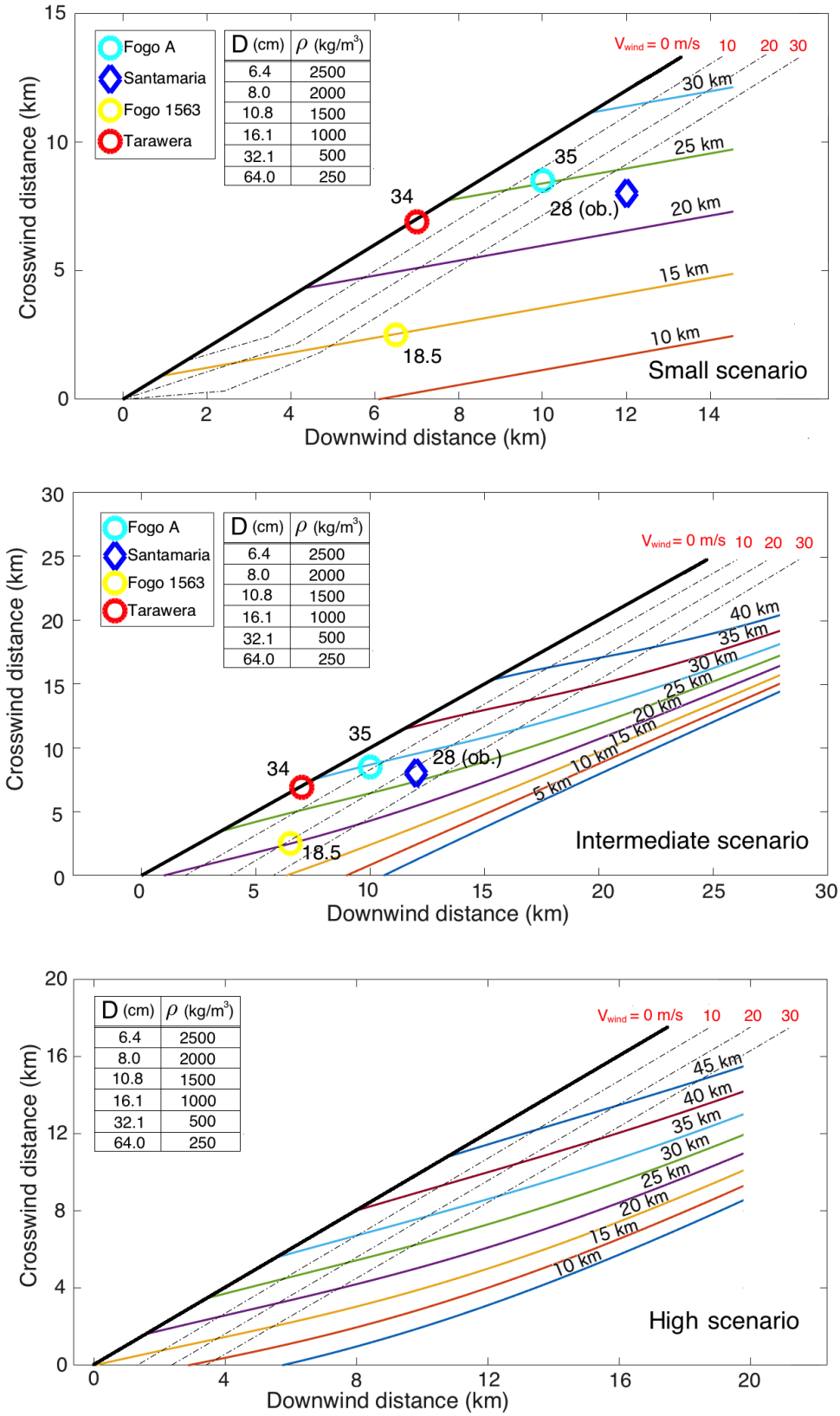

Figure S2: Nomograms for lithics of 6.4 cm of diameter and aerodynamically equivalent combinations of size and densities for 3 eruptive scenarios: low, intermediate and high intensity. Dot-dashed lines represent pairs of points characterized with same values of maximum wind at the tropopause (V_{wind}^{max}). Dashed lines on the left of the nomogram represent the horizontal lines of plume heights in CS86.

Supplementary material 4:

DEFINITION OF ERUPTIVE SCENARIOS

Table S2. Definition of the three eruptive scenarios applied to the compilation of the nomograms of Figures 8 and 9

Scenario	**Radius**
Low intensity	$r \leq 50\ m$
Intermediate intensity	$50\ m \leq r \leq 200\ m$
High intensity	$200\ m \leq r \leq 500\ m$

Supplementary material 5:

LIST OF MATHEMATICAL SYMBOLS

Table S3 List of mathematical symbols

Symbol	Definition	Unit
A	Projected area ($A \approx \frac{\pi}{4} d^2$) of a single clast	m^2
b	Gaussian width parameter $\frac{R^2}{b^2} = 2$	m
c_a	Specific heat capacity of the air	$J\ kg^{-1}K^{-1}$
c_b	Specific heat capacity of the mixture	$J\ kg^{-1}K^{-1}$
C_d	Drag coefficient	-
c_0	Zero-order coefficient of the Taylor series expansion for wind velocity as a function of the radial coordinate r	$m\ s^{-1}$
c_1	First-order coefficient of the Taylor series expansion for wind velocity as a function of the radial coordinate r	s^{-1}
d_c	Clast diameter	m
E_{tot}^{NBL}	Volumetric flow rate	$m^3\ s$
el	Clast elongation $el = \frac{I}{L}$	-
$\vec{F}_{drag}$	Drag force	N
$\vec{F}_g$	Gravitational force	N
fl	Clast flatness $fl = \frac{S}{I}$	-
g	Gravitational acceleration	$m\ s^{-2}$
h_{gc}	Height of the gravity current	m
H_{NBL}	Height of the Neutral Buoyancy Level (NBL)	m
h_{pb}	Maximum height of the plume used as benchmark for testing the effect of different latitudes	m
h_{pp}	Maximum plume height predicted by the nomograms	m
H_S	Height in the stratosphere where the CS86 wind profile assumes the constant value of $0.75\ V_{wind}^{max}$	m
H_T	Height of the tropopause	m
I	Intermediate length of the clast	m
K_1	Error in the Gaussian velocity profile of Eq.4 assuming a wind profile that not depends on r. K_1 holds under the hypothesis of a linear relation for wind velocity and radial coordinate, i.e. $V_{wind} \approx c_1 \cdot r + c_2$	$m\ s^{-1}$
k_N	Newton's drag correction factor	-
k_S	Stokes' drag correction factor	-
L	Longest length of the clast	m
MFR	Mass flow rate	$kg\ s^{-1}$
m_c	Mass of a single clast	kg
N	Atmospheric buoyancy frequency	s^{-1}
n_d	Mass fraction of dry gas component	-
n_s	Mass fraction of solid component	-

n_v	Mass fraction of water vapour component	-
P_{atm}	Atmospheric pressure	Pa
P_{sat}	Saturation pressure of water vapour	Pa
Q_d	Mass flow of dry air	$kg\ s^{-1}$
Q_s	Mass flow of solid phase	$kg\ s^{-1}$
Q_{tot}	Total mass flow $Q_{tot} = Q_d + Q_v + Q_s$	$kg\ s^{-1}$
Q_v	Mass flow of water vapour	$kg\ s^{-1}$
r	Radial coordinate along plume radius	m
r_h	Relative humidity	-
R	Top-hat radius of the plume	m
R_d	Gas constant of dry air	$J\ kg^{-1}\ mol^{-1}$
R_{env}	Radius of the clast support envelope	m
Re_p	Particle Reynolds number	-
R_g	Gas constant of the mixture	$J\ kg^{-1}\ mol^{-1}$
R_v	Gas constant of waer vapour	$J\ kg^{-1}\ mol^{-1}$
s	Curvilinear coordinate along the center-line of the plume	m
S	Shortest length of the clast	m
St	Stokes number	-
T_b	Plume temperature	K
$\vec{U}_c^i$	Velocity of the *i-esim* sedimenting clast	$m\ s^{-1}$
U_{entr}	Velocity of the entrained atmospheric air	$m\ s^{-1}$
$\vec{U}_f$	Velocity of the surrounding fluid for a sedimenting particle	$m\ s^{-1}$
U_g	Gaussian profile of plume velocity	$m\ s^{-1}$
U_g^*	Maximum value of plume velocity at the center line	$m\ s^{-1}$
U_{gc}	Velocity of the radial spreading of the umbrella cloud	$m\ s^{-1}$
U_{tv}	Terminal velocity of an object	$m\ s^{-1}$
U_{th}	Top-hat profile of plume velocity	$m\ s^{-1}$
V_{wind}	Modulus of wind velocity	$m\ s^{-1}$
$\bar{V}_{wind}$	Modulus of wind velocity	$m\ s^{-1}$
V_{wind}^{max}	Maximum value of the modulus of wind velocity at the tropopause	$m\ s^{-1}$
x	East-ward coordinate in the Cartesian system of reference	m
y	North-ward coordinate in the Cartesian system of reference	m
w_a	Mass ratio of water vapor to air in the atmosphere	-
w_s	Mass ratio of water vapor to air under saturated conditions	-
z	Vertical coordinate in the Cartesian system of reference	m
z_{max}	Maximum plume height	m
α_e	Entrainment coefficient along the axis of the plume	-
β_e	Entrainment coefficient along the radial component of the plume	-
Δ_h	Difference between the benchmark and the predicted height, normalized to the height of the benchmark, expressed as a percentage	%
Δ_v	Difference in height between vent altitude and the altitude of the field location at the downwind range	-
θ	Angle of the plume central axis respect to the ground	rad
λ	Geometrical correction factor for the gravity current	-

	$\lambda \approx 1$	
ρ_{atm}^{d}	Density of dry air	$kg\ m^{-3}$
ρ_{atm}^{v}	Density of water vapour	$kg\ m^{-3}$
ρ_b	Bulk density of the plume mixture	$kg\ m^{-3}$
ρ_c	Density of the clast	$kg\ m^{-3}$
ρ_f	Density of the fluid surrounding the clast	$kg\ m^{-3}$
ρ_{gas}	Density of the gas phase	$kg\ m^{-3}$
ρ_s	Density of the solid phase inside the plume model	$kg\ m^{-3}$
τ_f	Characteristic timescale of the fluid	s
τ_p	Response time of the particle	s
Φ_a	Azimuthal wind angle	rad

Supplementary material 6:

EFFECT OF DIFFERENT CLIMATE ZONES ON THE USE OF THE NOMOGRAMS

Plume rise depends on the density differences between the gas mixture and the atmosphere and thus, ultimately, on the atmospheric temperature. Different atmospheric profiles, notably different tropopause heights and temperature profiles, will affect both plume dynamics and sedimentation processes. Here we provide an estimation of the error associated with using the nomograms provided in this study, evaluated for a temperate profile, for eruptions characterized by different atmospheric profiles.

We tested two alternatives: a *tropical profile*, defined for latitudes between the 23rd parallels north and south of the equator with a tropopause height of 15 km, a surface temperature of 293 K and a moist adiabatic lapse rate in the troposphere of $-5.7\ K/km$. An *arctic profile*, defined for latitudes situated poleward from the 66th parallel, with a tropopause height of 8 km, a surface temperature of 273 K and a moist adiabatic lapse rate in the troposphere of $-8\ K/km$. Tropopause heights as a function of the latitude are reported in Shapiro et al. (1987).

Assuming the same wind profile as in CS86, for a maximum wind velocity at the tropopause of $30\ m/s$ the increase of wind velocities with height in the tropopause is faster in the Arctic region ($0.003\ s^{-1}$) than in the tropical one ($0.002\ s^{-1}$). Tests show that for the same initial conditions the arctic profile generally produces lower plume heights with respect to the standard and tropical profiles. However, the broader shape of the envelope under arctic conditions results in slightly larger sedimentation distances.

In the following discussion, we refer to the heights provided by the plume model as the *model height* (h_{pb}) and those evaluated with the nomograms as the *nomogram height* (h_{pp}). The

match between the model and the nomogram height provides an indication of the error associated in using nomograms with different atmospheric profiles with respect to the standard temperate. Tables S4 and S5 show the differences Δ_h in percentage between the benchmark and the predicted height for the arctic and tropical profile, respectively ($i.e. \Delta_h = 100 \times \left|\frac{h_{pp}-h_{pb}}{h_{pb}}\right|$). We notice that high intensity scenarios are less affected by the choice of the atmospheric profile ($\Delta_h = 7\%$) than low and intermediate intensity scenarios ($\Delta_h = 7 - 20\%$). A large MFR and initial radii reduce the relative importance of the atmosphere on the plume rise height. It is worth stressing that the uncertainties introduced by atmospheric conditions should be added to the intrinsic uncertainties associated with the model if nomograms are used for eruptions not located at a temperate latitude.

Size (mm)	**Intensity scenario**	Δ_h (%)			
		Wind @ tropopause(m/s)			
		0	**10**	**20**	**30**
16	Low/Intermediate	8%	10%	16%	12%
16	High	5%	6%	5%	7%
32	Low/Intermediate	18%	18%	20%	20%
32	High	5%	5%	6%	5%

Table S4 Arctic atmospheric profile. Differences between plume height predicted using the nomograms of Figures 8 and 9 and plume heights computed with the integral plume model, expressed in terms of the quantity Δ_h.

Size (mm)	**Intensity scenario**	Δ_h (%)			
		Wind @ tropopause (m/s)			
		0	**10**	**20**	**30**
16	Low/Intermediate	13%	12%	16%	20%
16	High	7%	7%	6%	7%
32	Low/Intermediate	9%	11%	13%	16%
32	High	8%	7%	7%	8%

Table S5 Tropical atmospheric profile. Differences between plume heights predicted using the nomograms of Figures 8 and 9 and plume heights computed with the integral plume model, expressed in terms of the quantity Δ_h.

[i] Radar observation, Vidal et al. (2017) (observation related to the 1st plume of Calbuco 2015, i.e. corresponding to Layer 1 of Castruccio et al. (2016)); [2] satellite (left value) and radar (right value) observations relatively to B2 phase, Holasek & Self (1995); [3] satellite observation, Holasek et al. (1996); [4] Visual estimation, Anderson (1908); [5] satellite observation, Maeno et al. (2014); [6] this prediction is based on the isopleth contour of 5 cm scoria clasts with a density of 1350 kg/m^3 (Castruccio et al., 2016; Layer 1) and our nomogram for particles with 5.3 cm and density of 1500 kg/m^3 (the Calbuco 2015 eruption was not reported in the nomograms of Figs 8 and 9 since clast size and density from field data do not perfectly match the combinations available in the plots); [7] plume height calculated using an average of 1.6 cm and 3.2 cm nomograms, both for CS86 and the present work (maximum downwind and crosswind ranges are associated with lithic clasts of the B2 phase; Carey et al. (1990)); NA: not available.